UNIVERSIDAD DE CONCEPCIÓN
FACULTAD DE CIENCIAS FÍSICAS Y MATEMÁTICAS

AN UPGRADE TO THE 230 GHz CSO BALANCED RECEIVER ARCHITECTURE FOR THE FIRST LIGHT LCT RECEIVER

Por: Miguel Angel López Remolcoy

Tesis presentada a la Facultad de Ciencias Físicas y Matemáticas de la Universidad de Concepción para optar al grado académico de Magíster en Astronomía

Noviembre 2023
Concepción, Chile

Profesor Guía: Dr. Rodrigo Reeves
Co-guía: Dr. Miguel Martínez Ledesma

Dedicado a mis padres.

Acknowledgments

En primer lugar, agradezco a mi familia por su constante apoyo en esta gran etapa universitaria, por su ayuda, consejos, por levantarme el ánimo en momentos difíciles, y por confiar siempre en mi.

Debo agradecer también a mis profesores Rodrigo Reeves y Miguel Martínez por su guía en el trabajo de esta tesis. También agradezco a Jacob Kooi por proveer los materiales necesarios para la realización de esta tesis, y por las importantes sugerencias que dieron nuevas luces sobre cómo abordar los objetivos.

Agradezco también a mis compañeros de CePIA por su buena disposición al momento de ayudarme con ciertos conceptos, y por hacer mas entretenidos los días de trabajo en el "lab".

Por último, la realización de esta tesis fue gracias al proyecto CASSACA.

Contents

List of Tables

List of Figures

Acronyms

- ADC: Analog to Digital Converter.
- ALMA: Atacama Large Millimeter/Submillimeter Array.
- AOS: Acoustic-Optic Spectrometer.
- APEX: Atacama Pathfinder Experiment.
- AWR: Applied Wave Research.
- BPF: Band-pass filter.
- CePIA: Centro Para la Instrumentación Astronómica.
- CALTECH: California Institute of Technology.
- CSO: Caltech Submillimeter Observatory.
- DC: Direct Current.
- DSB: Double Sideband.
- EMI: Electromagnetic Interference.
- FFTS: Fast Fourier Transform Spectrometer.
- FPGA: Field Programable Field Array.
- HFSS: High Frequency Software Simulator.
- IF: Intermediate Frequency.
- ISM: Interstellar medium.
- IGM: Intergalactic medium.
- JMCT: James Clerck Maxwell Telescope.
- LCT: Leighton Chajnantor Telescope.
- LNA: Low Noise Amplifier.
- LO: Local Oscillator.

- LSB: Lower Sideband.
- RF: Radio Frequency.
- SIS: Superconductor Insulator Superconductor.
- 2SB: SideBand Separation.
- SMA: SubMiniature Version A Connector.
- SRR: Sideband Rejection Ratio.
- TEM: Transverse Electromagnetic.
- T_R: Noise Temperature of the Receiver.
- T_{sys}: System Temperature.
- TZ: Transmission Zero.
- UdeC: Universidad de Concepción.
- USB: Upper Sideband.
- VNA: Vector Network Analyzer.

Abstract

The Leighton Chajantor Telescope (LCT) is an international collaboration between China, the USA, and Chile, that looks for the participation of scientists and engineers from the three nations in the development of frontier technologies for submillimeter astronomy. Also, the LCT is the first radio telescope that will be operated, managed, and upgraded in collaboration with a Chilean Institution. The project considers the upgrade of the Caltech Submillimeter Observatory (CSO), which is currently decommissioned in Mauna Kea, Hawaii, and will be moved to the Chajnantor area, in northern Chile, one of the best places in the world for submillimeter astronomy due to its low levels of water vapor in the atmosphere.

In particular, one of these upgrades is a modification of the architecture of the receiver. Its original design is based on a DSB architecture that generates a superposition of the sidebands, leading to an important noise contribution to the IF signal response, this results in less sensitivity, therefore the telescope will require more integration time during the observations. This receiver was designed to cover the 180-720 GHz frequency range through two independent receiver blocks. In this study, it will be considered the upgrade of the receiver that covers the 230-460 GHz frequency band.

This thesis (framed within a CASSACA project) proposes to evaluate the design of a new configuration for the receiver and evaluate the feasibility of converting the DSB to a 2SB system. This will reduce the noise level by removing the contribution of the image band, improving the receiver sensitivity. Simulations in HFSS and AWR of the previous DSB configuration were made, in order to compare and develop a model that can be modified and analyzed. The results of the modification to the circuit show that it is possible to expand the bandwidth in which the receiver works, from the previous 4 GHz to 9.3 GHz. On the other hand, the theoretical study of the feasibility of the application of a 2SB configuration in the circuit, allowed us to elucidate that it is not possible to directly implement the 2SB architecture on the DSB system due to the limitations imposed by the input signals to the module.

Keywords – Receiver, DSB, 2SB, Bandwidth

Resumen

El Leighton Chajnantor Telescope (LCT) es una colaboración internacional entre China, EEUU, y Chile que busca ampliar la participación de científicos e ingenieros de las tres naciones en el desarrollo de tecnologías de última generación para la astronomía submilimétrica. Además, el LCT es el primer radiotelescopio que será operado, gestionado, y mejorado en colaboración con instituciones chilenas. El proyecto considera la actualización del Caltech Submilimiter Observatory (CSO), que actualmente se encuentra decomisionado en Mauna Kea, Hawái, y su traslado al Llano de Chajnantor, en el norte de Chile, uno de los mejores lugares del mundo para la astronomía submilimétrica debido a sus bajos niveles de vapor de agua en la atmósfera.

En particular, una de las actualizaciones del LCT es el cambio de arquitectura del receptor. El diseño actual basado en la arquitectura DSB que genera una superposición de las bandas laterales, provocando una importante contribución de ruido a la señal IF, resultando en menor sensibilidad, y por lo tanto se requiere de mayor tiempo de integración durante la observación. Este receptor fue diseñado para cubrir el rango de frecuencias 180-720 GHz mediante dos receptores independientes. En esta tesis se trabajará con el receptor que cubre ventanas espectrales con bandas en 230-460 GHz.

Esta tesis (enmarcado en un proyecto CASSACA) propone evaluar el diseño de una nueva configuración para el receptor, determinando si es posible modificar el actual diseño DSB para convertirlo en un sistema 2SB. Esto reduciría el nivel de ruido base al eliminar la contribución de la banda imagen, mejorando la sensibilidad del receptor. Para lograr ese objetivo, se realizó una simulación del funcionamiento de la configuración original (DSB) usando los software HFSS y AWR. Los resultados de la simulación de las diversas mejoras y modificaciones sobre el circuito original, muestran un ancho de banda mejorado en la señal IF resultante, pasando de 4 GHz a 9.3 GHz. Por otro lado, el estudio teórico de factibilidad de la aplicación de una configuración 2SB en el circuito, permitió dilucidar que no es posible llevarlo a cabo directamente debido a la forma en que están diseñadas las entradas de las señales del módulo.

Keywords – Receiver, DSB, 2SB, Bandwidth

Chapter 1

Introduction

Nowadays, two different types of observatories exist for millimeter and submillimeter signals. The first type is the antenna array, which utilizes interferometric techniques. In this technique signals from two or more antennas can be combined, allowing these antennas to observe the same astronomical source and apply the superposition principle to obtain high-angular-resolution images. The most renowned example of an interferometric observatory is the Atacama Large Millimeter/Submillimeter Array (ALMA) where up to 66 antennas are used simultaneously. Increasing the distance between the multiple antennas enhances angular resolution. The signals from these antennas are combined and processed to synthesize the functionality of a large individual radio telescope (ALMA, 2021). However, a significant drawback of such arrays is the substantial funding required for their development, making these projects almost inaccessible to most institutions.

The other type of observatory is based on single-dish radio telescopes. Although this kind of observatory does not offer the angular resolution of an interferometric array, it comes with several advantages. These include simpler electronics requirements compared to an array, a high-velocity mapping rate, ease of upgrading, and the potential to be integrated into an array. Some examples of these observatories include the Atacama Pathfinder Experiment (APEX), the Caltech Submillimeter Observatory (CSO), and the James Clerck Maxwell Telescope (JMCT).

In particular, the Caltech Submillimeter Observatory (CSO), a decommissioned

single-dish radio telescope located on Mauna Kea, as shown in figure 1.0.1, has been employed for studying molecular gas and dust particles in the densest regions of the interstellar medium (ISM). These regions are where stars form through the gravitational collapse of molecular clouds. In this context, submillimeter waves allow the study of star formation due to their ability to penetrate dust clouds. The CSO has also contributed to extragalactic astronomy, providing key information to determine the history of star formation. In fact, the light received by the CSO from the most distant galaxy was emitted approximately 12 billion years ago (Golwala, 2023).

The CSO will be relocated to Chile and undergo an upgrade to pave the way for the Leighton Chajnantor Telescope (LCT). The benefits of having this radio telescope in Chile are diverse. Astronomers from Chilean universities will have unprecedented access to develop their scientific goals. Additionally, it offers the opportunity to participate in the development of state-of-the-art submillimeter instrumentation. It will also play a vital role in training the next generation of astronomers and engineers within the Chilean scientific community.

The scientific goals of the new LCT are not very different from those of the CSO. For example, one of the goals is to create cold dust maps of nearby galaxies to isolate star formation structures and trace their origin within the galaxy's structure. Another important use for the LCT is the study of the intergalactic medium (IGM) of galaxy clusters to determine the physics behind their growth. Additionally, the LCT will serve as a technological development center, where the current project involving the upgrade of the receiver will be carried out.

Technically, a heterodyne system translates the frequency at which the cosmic signal travels from the source, into a technologically manageable resultant frequency called: the intermediate frequency, or IF. The proposed receiver upgrade involves modifying the architecture of the IF circuit board and assessing the feasibility of transitioning from the current Double Sideband (DSB) scheme to a Sideband Separating (2SB) configuration. Furthermore, this modification involves expanding the bandwidth of the IF circuit by incorporating passive components. This would constitute a significant contribution to the general objective of upgrading the LCT.

The effectiveness of the 2SB system has already been demonstrated at the

Chajnantor site. Iguchi (2005) recommends implementing the 2SB architecture for all ALMA bands, highlighting its numerous advantages over the DSB scheme. These advantages include improvements in calibration methods, spectral line observations, and polarization observations. Specifically, for spectral line observations in the presence of atmospheric background, rejecting the unused sideband can reduce the integration time required to achieve a certain level of signal-to-noise ratio by a factor of two. This integration time increase has large operational implications in terms of cost and observation capabilities due to the requirement to observe the same source twice the time.

Moreover, Khudchenko et al. (2012) evaluated the upgrade of the ALMA band 9 receiver from the DSB architecture to a 2SB scheme, verifying that the integration time required for spectral line observations is reduced by a factor of two. The technology employed in their receiver utilizes SIS mixers. The sideband rejection ratio is 15 dB, meeting ALMA specifications of 10 dB for this band.

To effectively achieve sideband separation, FPGA-based platforms have been evaluated as backend digital components. Finger et al. (2013), demonstrated that using this kind of platform, it is possible to achieve a sideband rejection ratio (SRR) that is sufficiently good for its usage in spectral line observations. In this thesis, a 90° hybrid digitally implemented at the IF signal output is proposed, and the analysis of the sideband separation is numerically assessed. The primary advantage of using a digital development platform, i.e. an FPGA for sideband separation, is the ability to correct phase and gain imbalances that may exist in each branch of the circuit.

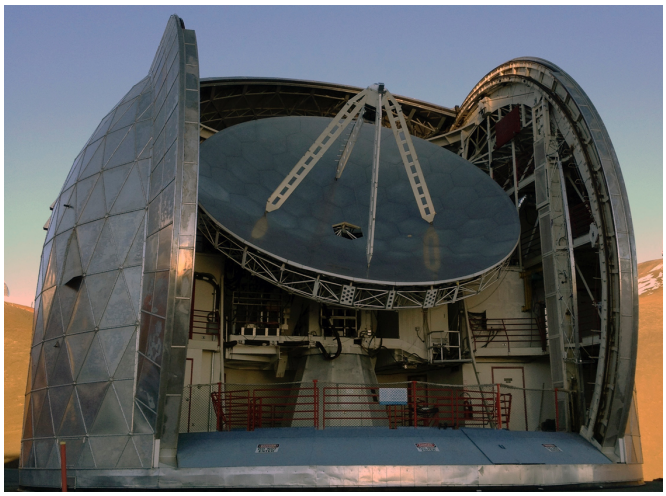

Figure 1.0.1: Radio telescope CSO, the next LCT (Golwala, 2023).

1.1 Thesis Proposal

1.1.1 Hypothesis

In this research, the primary challenge we are addressing is the limited bandwidth of 4 GHz imposed by the IF circuit board of the receiver. Moreover, the current heterodyne SIS receiver operates in a Double sideband (DSB) configuration, which increases the IF noise level, thereby diminishing sensitivity and increasing observation time.

"An enhancement of the observing capabilities of the Leighton Chajnantor Telescope is possible, through the modification of the current Caltech Submillimeter Observatory 230/460 GHz IF receiver circuit."

1.1.2 Proposed solution

The objective is to improve the bandwidth of the IF circuit by incorporating passive components and removing elements from the current circuit board. This modification aims to increase the IF bandwidth of the LCT receiver to 9 GHz instantaneous at baseband. For this purpose, we plan to use 3D modeling and simulation in specialized RF/electromagnetic software, such as HFSS and AWR.

Another objective is to implement a 2SB architecture in the IF circuit to eliminate the noise contribution from the image band. A mathematical analysis is conducted to assess the feasibility of the 2SB configuration in the IF circuit board of the LCT receiver. This change is anticipated to reduce integration time during the observations by aggresively attenuating unwanted atmospheric contributions from the sidebands.

In summary, this project aims to contribute to the upgrade of the LCT receiver technology, providing new capabilities to this crucial observatory for the Chilean astronomical community.

1.1.3 Objectives

• **General Objectives**

Design and simulate an IF circuit board to upgrade the Leighton Chajnantor Telescope receiver to enhance its observation capabilities, i.e. reduce the integration time by a factor of two, only considering electronic noise, and substantially improve the IF bandwidth.

• **Specific Objectives**

1. Understand the functionality of the 230/460 GHz CSO receiver, and learn the requiered software tools for the analysis/design.
2. Modify the CSO receiver configuration.
3. Design a new architecture for the IF circuit of the LCT receiver.
4. Simulate the performance of the new IF circuit design.
5. Increase the IF bandwidth of the LCT receiver, from 4 GHz to 9 GHz bandwidth.
6. Investigate the feasibility of implementing a 2SB configuration in the IF circuit through mathematical analysis.

1.1.4 Methodology

In order to achieve the objectives of this project, the necessary steps are listed as follows:

- Aquire information of the CSO receiver, including previous designs and simulations.
- Model previous designs using 3D modeling software.
- Perform EM simulations of this replicates for the existing system.
- Once the CSO simulation results are achieved, start with the modification of the CSO IF circuit to build the new IF circuit design of the LCT receiver.
- Explore the best passive component options to install in the circuit.

- Aquire the S-parameters of the passive components from the manufacturer's websites.
- To construct the IF circuit, modify the transmission lines, and integrate the S parameters of passive components into the HFSS model of the IF circuit.
- Validate the performance of the new components through simulations in AWR and HFSS.
- Validate the performance of the new circuit design through simulations in HFSS.
- Describe mathematically the performance of the CSO receiver.
- Describe the 2SB architecture mathematically.
- Demonstrate analytically the feasibility of a 2SB architecture in the LCT IF circuit.

1.2 Thesis Outline

This thesis focuses on the modification of the CSO receiver and the design of a new IF circuit for the LCT receiver. It includes the following chapters:

Chapter 2: This chapter elucidates the theory underlying IF circuits and receivers. The first section introduces the general concepts and receiver components. The second part delves into the characteristics and current state of the CSO receiver. The third section covers the topics related to the planned LCT receiver concepts.

Chapter 3: The third chapter of this thesis explores the requirements and essential tools for designing the new LCT receiver. It also outlines the prerequisites for the analytical model of the proposed modifications to the CSO receiver.

Chapter 4: This chapter centers on presenting the results of this thesis and how they were achieved. It includes the 3D modeling of the CSO and LCT receivers using specialized software, along with simulations showcasing their performance.

Chapter 5: The final chapter discusses the receiver design and simulations, sideband separation studies, and the hypothesis proposed in this thesis. It also provides a summary of conclusions and outlines directions for future work.

Chapter 2

Fundamentals of the CSO and LCT Receivers

2.1 Receivers, an overview.

In general, coherent receivers used in radioastronomy are divided into two main parts: front-end and back-end, which dividing points are in some way arbitrary (Wilson et al., 2008). The front-end is commonly based on an initial low noise amplifier (LNA) operating at the frequency of the signal coming from the sky. Amplifiers are necessary to increase the faint signal levels of the incoming signals. Then, a mixer is used as a frequency converter. The mixer performs the displacement of the acquired signals to lower frequencies where they can be correctly processed. When the initial LNA is not available at the input frequency (because its gain, noise, or bandwidth are not required for the correct operation), the mixer is used as the first component of the input chain. Usually, front-end electronic components operate at cryogenic temperatures to diminish their internal noise. On the other hand, the back end operates at lower frequencies. These devices are in charge of the signal conditioning and conversion to digital to be analyzed. Besides, the back-end typically performs the spectral properties of the incident signal.

The most common receiver architecture is the super-heterodyne, where the signal collected by the antenna is guided to the front-end. At the front-end, the signal passes through a radio frequency (RF) amplifier, then it passes through a mixer

where the signal is mixed with a local oscillator (LO) signal. Here the RF signal is converted to an intermediate frequency (IF), which corresponds to the difference between the RF and LO frequencies. In our case, the intermediate frequency is on the order of a few GHz, while the RF and LO are around 350 GHz. The low frequency of the IF makes it easier to handle for digitalization. The power of the IF signal is directly proportional to the RF signal power (Kraus et al., 1986), preserving the integrity of the incoming cosmic signal.

After the mixer, the signal passes through a band pass filter, to remove the spurious signals that have been introduced at frequencies different than the IF band by the mixer. These undesired signals (located at frequencies outside of the IF band) reduce the performance of the system and can interfere with other modules of the same system. Finally, the front-end's last stage is amplifying the IF signal to adapt the signal to the required voltage levels at the output. The general scheme of the receiver explained in this section is shown in figure 2.1.1. The resulting IF signal now enters the back end, where it can be analyzed by an acoustic-optic (AOS) spectrometer, or by a fast Fourier transform spectrometer (FFTS) (Kooi, 2008).

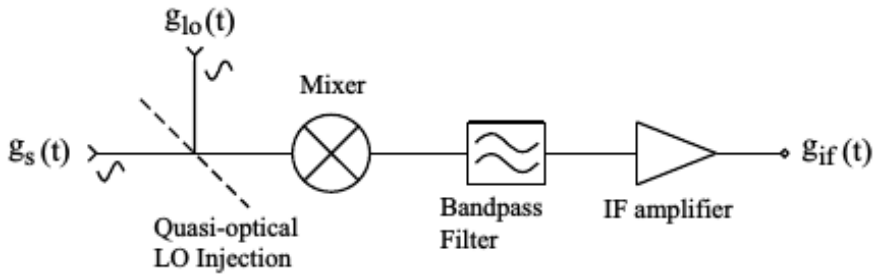

Figure 2.1.1: Heterodine receiver scheme (Kooi, 2008).

The mixer situated in the front end generates a product of the two input signals, hence the target signal ($g_s(t)$) is multiplied by the LO signal ($g_{lo}(t)$):

$$g_s(t) \cdot g_{lo}(t) = V_s cos(w_s t + \phi_s) \cdot V_{lo} cos(w_{lo} t + \phi_{lo}) \tag{2.1.1}$$

The result, once the signal passes through the band pass filter (selecting only low frequencies) is the Intermediate Frequency (IF) signal:

$$g_{IF}(t) = cos(|w_s - w_{lo}|t \mp \phi_{IF}) \tag{2.1.2}$$

Note that the equation 2.1.2 considers the case in which an ideal mixer with unity gain is used, and $V_s = V_{lo} = 1$. From this equation, it can be seen that if the frequency of the signal is bigger than the LO frequency ($w_s > w_{lo}$), then the intermediate frequency is positive, in this case, it is indicated that the signal will be in the upper side band (USB). On the other hand, if the frequency of the signal is smaller than the LO frequency ($w_s < w_{lo}$), then the intermediate frequency is mathematically negative, hence we consider that the signal will be in the lower side band (LSB). It is relevant to highlight that the sideband where the signal resides is identified as the 'signal' band, leaving the other as the 'image' band (Kooi, 2008).

Another important parameter of the receiver is the IF bandwidth. The relevance of this parameter is that a larger bandwidth allows for observing more molecular lines simultaneously. A large bandwidth allows the direct analysis of wide emission lines with extragalactic origin. Figure 2.1.2 shows an example of Orion KL spectra, taken by CSO. The measured spectrum, with a bandwidth of 4 GHz allows identifying several molecular lines.

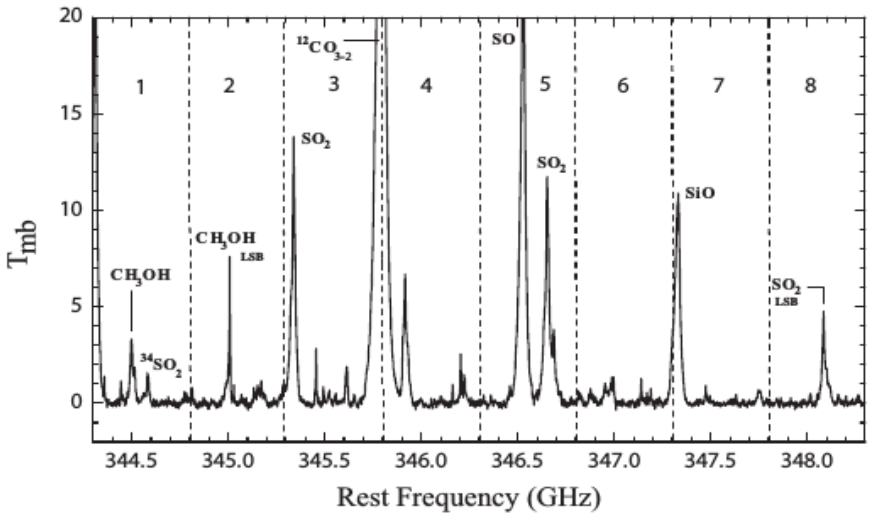

Figure 2.1.2: Orion KL spectra, star formation region inside Orion nebula (Kooi, 2008).

2.1.1 Balanced Mixer

Two single-ended mixers that are reversed and combined with a hybrid junction can make a balanced mixer (or balanced receiver). The hybrid junction can be either a 90° or a 180° hybrid, and the basic configuration is shown in figure 2.1.3.

The benefit of using a 180° hybrid is the perfect RF and LO isolation over a wide frequency range. A 90° hybrid can cause an LO signal that reflects off the active device to appear at the RF port, which can cause local oscillator-induced optical standing waves in the telescope structure. This standing wave can create gain instability at the output of the receiver (Kooi, 2008). The benefit of using a 90° hybrid is that it can ideally provide a perfect input match at the RF port over a wide frequency range.

The model used in the CSO receiver is a 90° hybrid due to its simplicity of fabricating in a small space, such as in the module of the receiver.

We can represent the non-linearity of the mixer diodes, $i_1(t)$ and $i_2(t)$, with a Taylor series expansion as follows:

$$i_1(t) = \sum_{n=0}^{\infty} \frac{K_n V_1(t)^n}{n!} \tag{2.1.3}$$

As we have two mixers, those devices are placed in opposite polarity, hence $V_2(t) = -V_1(t)$, in this case the current is represented by:

$$i_2(t) = \sum_{n=0}^{\infty} (-1)^n \frac{K_n V_2(t)^n}{n!} \tag{2.1.4}$$

With K_n the mixer gain.

In subsection 2.2.3.2 we treat the theory and implementation of the balanced mixer in the current receiver. In particular, the design of the module with a quadrature hybrid constructed in waveguide.

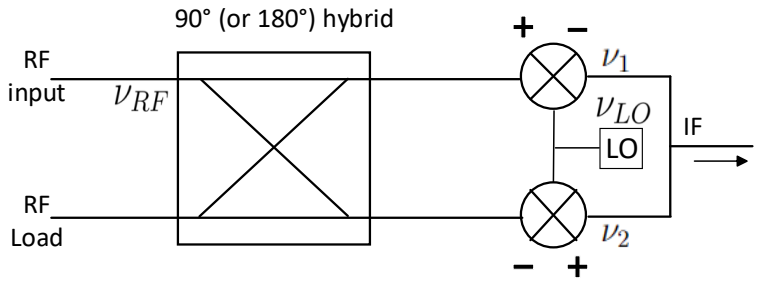

Figure 2.1.3: Balanced receiver scheme, it can be composed by either a 90° or a 180° hybrid and two single-ended mixers.

2.1.2 Scattering Matrix

Direct measurements of voltages and currents at microwave frequencies are usually difficult because they require the magnitude and phase of a wave moving in a specific direction or of a standing wave. A representation that is more consistent with direct measurements, and with the concepts of incident, reflected, and transmitted waves, is given by the scattering matrix or S-parameters.

The voltage waves that enter and leave the ports of a network are related by the S-parameters, which give a complete description of a network. They can be measured directly using a vector network analyzer (VNA) or calculated using network analysis techniques. Once the scattering parameters of the network are known, conversion to other matrix parameters can be done.

Figure 2.1.4 shows a microwave network with N ports, which can be any kind of transmission line or a waveguide. The ports in the figure may be any type of transmission line or a waveguide. The voltage wave that enters the port n is V_n^+, and V_n^- is the voltage wave reflected from the port n. The scattering matrix, or [S] matrix, is defined based on these waves as in equation 2.1.5 (Pozar, 2011).

$$\begin{bmatrix} V_{lo}^- \\ V_1^- \\ \vdots \\ V_N^- \end{bmatrix} = \begin{bmatrix} S_{11} & S_{12} & \cdots & S_{1N} \\ S_{21} & S_{22} & \cdots & S_{2N} \\ \vdots & \vdots & \ddots & \vdots \\ S_{N1} & S_{N2} & \cdots & S_{NN} \end{bmatrix} \begin{bmatrix} V_1^+ \\ V_2^+ \\ \vdots \\ V_N^+ \end{bmatrix} \tag{2.1.5}$$

An element of the [S] matrix can be determined as in equation 2.1.6.

$$S_{ij} = \left. \frac{V_i}{V_j} \right|_{V_k^+ = 0 \; for \; k \neq j} \tag{2.1.6}$$

Equation 2.1.6 indicates that every element of the matrix can be determined by driving port j with an incident wave of voltage V_j^+, and measuring the reflected wave amplitude V_i^- coming out of port i. The incident waves on all ports are zero except for the jth port, which means that all ports should be terminated in matched loads to avoid reflections. Then, S_{ii} corresponds to the reflection coefficient seen at port i when all other ports are terminated in matched loads, and Sij is the transmission coefficient from port j to i when all other ports are

terminated in a matched load.

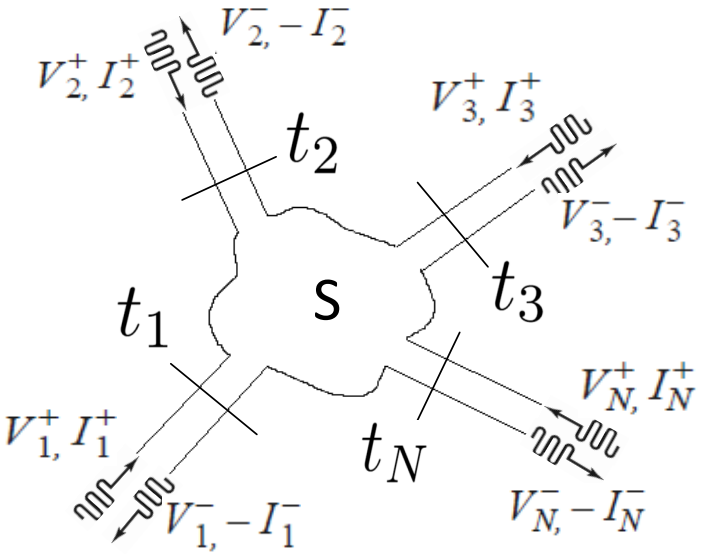

Figure 2.1.4: Arbitrary N-port microwave network.

2.1.3 The Quadrature 90° Hybrid

The quadrature hybrids are directional couplers that receive the RF and LO signals (in the case of the CSO receiver). This component generates output signals that are displaced by 90° out of phase at each of their ports. Figure 2.1.5 shows a simulation of the microwave behavior of this component installed in the current receiver.

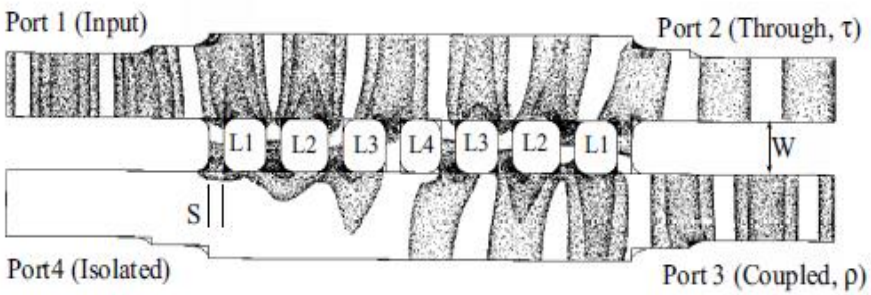

Figure 2.1.5: 90° hybrid design, constructed in the CSO receiver block. S denotes the branch line width ($S = 74\mu m$), W is the separation between the two waveguides ($W = 203\mu m$), L_n is the length between the branch lines ($L_1 = 205\mu m$, $L_2 = 231\mu m$, $L_3 = 205\mu m$, $L_4 = 190\mu m$)(Kooi, 2008).

The hybrid scattering matrix is shown in the following equation.

$$\left[S\right] = -\frac{1}{\sqrt{2}} \begin{bmatrix} 0 & j & 1 & 0 \\ j & 0 & 0 & 1 \\ 1 & 0 & 0 & j \\ 0 & 1 & j & 0 \end{bmatrix} \tag{2.1.7}$$

The ideal performance of a hybrid is shown in figure 2.1.6. The isolation between ports 1 and 4 (S_{14}) has to be perfect at the design frequency f_0, same as refelection loss (S_{11}). On the other hand, transmission from port 1 to ports 2 and 3 (S_{12} y S_{13}) has to be maximum for the frequency f_0. These values degrade as the frequencies move away from f_0.

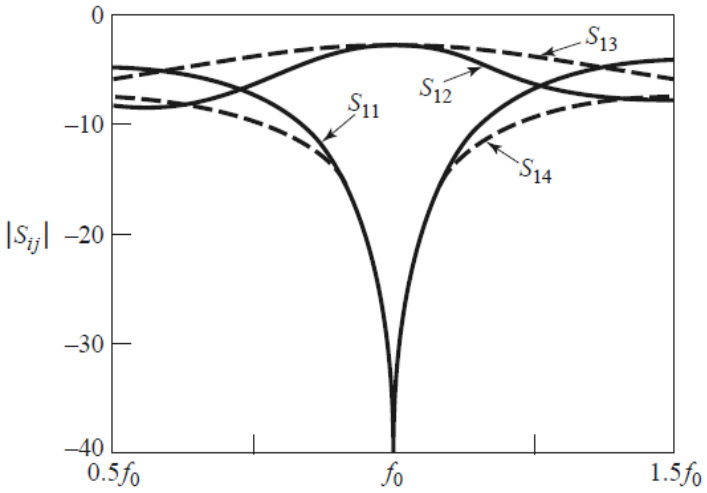

Figure 2.1.6: Ideal performance of a hybrid (Pozar, 2011).

The scheme shown in figure 2.1.7 represents a hybrid, which can be used to make the calculations of the output signals.

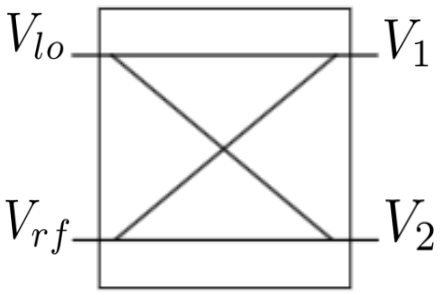

Figure 2.1.7: Hybrid representation with input and output voltages.

Let us consider V_{lo} and V_{rf} are the waves incident to the ports of the hybrid, $-V_{lo}$ with $-V_{rf}$ as the waves reflected from the ports. The output voltages are represented as V_1 and V_2, as shown in figure 2.1.7. We can calculate the output signals in the following form:

$$\begin{bmatrix} -V_{lo} \\ -V_1 \\ -V_2 \\ -V_{rf} \end{bmatrix} = -\frac{1}{\sqrt{2}} \begin{bmatrix} 0 & j & 1 & 0 \\ j & 0 & 0 & 1 \\ 1 & 0 & 0 & j \\ 0 & 1 & j & 0 \end{bmatrix} \begin{bmatrix} V_{lo} \\ V_1 \\ V_2 \\ V_{rf} \end{bmatrix} \tag{2.1.8}$$

Performing the matrix multiplication yields:

$$-V_{lo} = -\frac{1}{\sqrt{2}}(j \cdot V_1 + V_2) \tag{2.1.9}$$

$$-V_1 = -\frac{1}{\sqrt{2}}(j \cdot V_{lo} + V_{rf}) \tag{2.1.10}$$

$$-V_2 = -\frac{1}{\sqrt{2}}(V_{lo} + j \cdot V_{rf}) \tag{2.1.11}$$

$$-V_{rf} = -\frac{1}{\sqrt{2}}(V_1 + j \cdot V_2) \tag{2.1.12}$$

Here, we obtain V_1 and V_2 as:

$$V_1 = \frac{1}{\sqrt{2}}(j \cdot V_{lo} + V_{rf}) \tag{2.1.13}$$

$$V_2 = \frac{1}{\sqrt{2}}(V_{lo} + j \cdot V_{rf}) \tag{2.1.14}$$

Multiplying by the unit j induces a phase shift of $\pi/2$ for each signal. Subsequent calculations are conducted in section 2.2.3.1 to illustrate the hybrid's performance within the RF module of the receiver.

2.1.4 Filters

Filters are devices that change the phase of an input signal or limit the frequencies that go through a system. These devices stop unwanted signals outside the operating bandwidth of the application while letting in-band signals pass through

to the rest of the chain. Filters can be described by their response, which is the general shape of the S_{21} curve in the passband, transition, and stopband (Mini-Circuits, 2020). In figure 2.1.8, we can observe an ideal filter behavior, exhibiting 0 dB insertion loss in the passband, infinite rejection beyond the frequency cut-off f_c, and a transition from the passband to the stopband in 0 Hz.

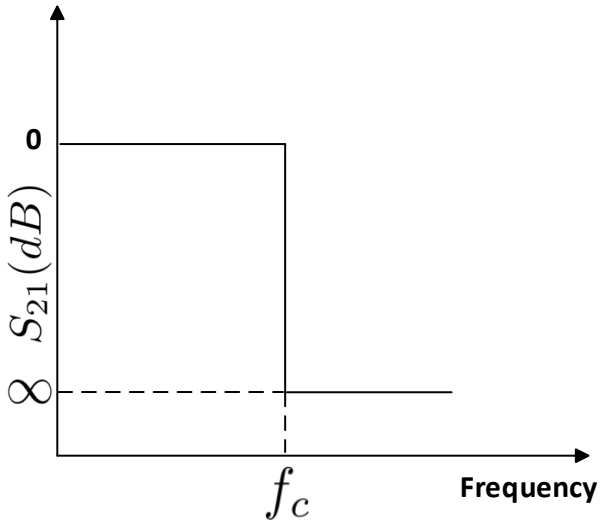

Figure 2.1.8: Ideal filter behavior. f_c is the frequency cut-off. The transmission is described by the S_{21} parameter in dB.

Filters can be grouped into a number of categories, the most common are the following:

- Bandpass filter:
  The frequencies allowed are a range between $f_{min} < f < f_{max}$.
- High pass filter:
  The range of frequencies allowed here is $f > f_{max}$.
- Low pass filter:
  The frequencies in this filter are up but not beyond a specified frequency, $0 < f < f_{max}$.
- Band Stop filter:
  Eliminates a range of frequencies from the system, $f_{min} < f < f_{max}$.
- All pass filter:
  Allows all the input frequencies, but changes the phase of the signal.

These filters can be either analog or digital. Low pass filters let frequencies go through unchanged to the digitalization and sampling stage. In practical systems, the DC term is not passed to avoid large offsets.

2.1.5 The Amplifier

A signal amplifier is a circuit that uses electrical power to increase the amplitude of an incoming signal voltage or current signal, and output this higher amplitude version at its output terminals. The ideal signal amplifier creates an exact replica of the original signal that is larger but identical in every other way. In practice, an ideal amplifier is not possible, because no circuit can perfectly and proportionately scale up all aspects of a signal past a certain point. The difference between the ideal amplification and the actual amplification is the gain error.

The power amplifier is usually the primary consumer of DC power, so amplifier efficiency is a crucial concept. One measure of this is the ratio of output power to DC input power. This quantity is sometimes referred to as drain efficiency and is defined as in equation 2.1.15 (Pozar, 2011).

$$\eta = \frac{P_{out}}{P_{DC}} \tag{2.1.15}$$

2.1.6 Friis Formula

This equation tells us about the noise temperature of a system due to the individual contribution of noise temperature from each component in cascade. The noise temperatures of the components are T_1, T_2,..., T_n; and the power gains are G_1, G_2,..., G_n. In figure 2.1.9 we can see a linear two port components in cascade connection, we can describe the noise temperature of this system as follows:

$$T = T_1 + \frac{T_2}{G_1} + \frac{T_3}{G_1 G_2} + ... + \frac{T_n}{G_1 ... G_{n-1}} \tag{2.1.16}$$

The previous formulation is known as the Friis equation (Friis, 1944), which indicates that the power gain of each component is large enough, the noise temperature of the system is mainly determined by the first component. This shows the importance of selecting the first component with low noise and high gain.

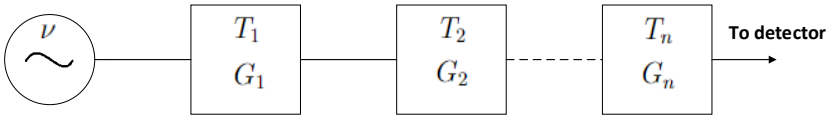

Figure 2.1.9: Linear two port components in cascade connection. A voltage ν is injected into the circuit components in cascade. The signal finally exits to the detector or the analog-to-digital converter.

2.1.7 Noise Temperature

Noise temperature is the amount of noise that the system adds to the signal that is received. By connecting a resistor R to the input terminals of a linear amplifier, we can relate electrical power and temperature. The thermal random motion of the electrons in the resistor will create a current $i(t)$ that can be measured. This power is determined by the physical temperature in thermal equilibrium, and this is called Johnson noise.

At any temperature above 0 K, the thermal noise power generated in a conductor is proportional to its absolute physical temperature. Then the thermal noise power is related to the noise temperature by:

$$P_N = kB(T_N + T) \tag{2.1.17}$$

where P is the power (watts), k is the Boltzmann's constant (J/K), B is the bandwidth (hertz), T_N is the noise temperature and T is the physical temperature of the device which produces the noise (Meyers, 2002).

2.1.8 Circuit Transmission Line

In this thesis, we will work with an IF circuit with a planar design. The reason for this is that its transmission line corresponds to a microstrip line printed over a substrate. A microstrip line is a common kind of flat transmission line in microwave circuits mainly because it can be fabricated by photolithographic processes and can be easily reduced in size and combined with both passive and active microwave devices.

A metal strip of width W is printed on a thin, grounded dielectric substrate of thickness d and relative permittivity ϵ_r. The shape of a microstrip is shown in

Figure 2.1.10.

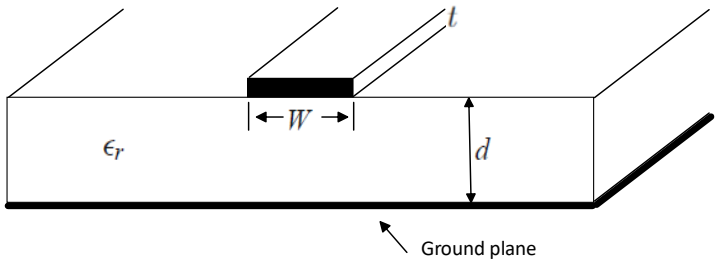

Figure 2.1.10: Geometry of a microstrip line over a substrate of relative permittivity ϵ_r and thickness d, W is the metal strip width, and t is the metal strip height. Below the substrate is the ground plane.

A microstrip line has a single-ended structure, meaning that the conductor shape is not symmetrical, and the one conductor, which is the ground plane, also usually acts as the ground for the source and load. The material between the conductors is usually a low-loss dielectric material with permeability close to that of free space ($\mu \approx \mu_0$) and relative permittivity ϵ_r. A microstrip line normally has a transverse electromagnetic (TEM) field pattern, which is shown in figure 2.1.11. Note that the electric and magnetic fields are present both in the dielectric and in the space above it, which is typically air (Ellingson, 2018).

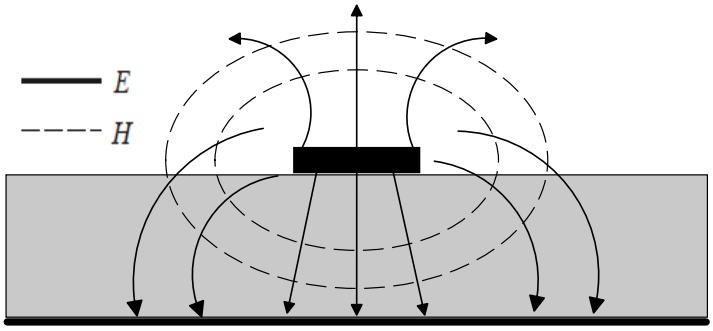

Figure 2.1.11: Sketch of the field lines of a microstrip. E is the electric field directed toward the ground plane, and H is the magnetic field.

The behavior and analysis of the microstrip line are more complex because of the dielectric, especially the fact that the dielectric does not fill the space above the strip. Expressions for Z_0 directly in terms of d/W and ϵ_r are typically used. A variety of these expressions are in common use, representing different approximations and simplifications. The equation 2.1.18 (Bogatin, 2020) for the

characteristic impedance Z_0 of microstrip with air above, and rectangular cross-section, propagation delay T_{pd}, and intrinsic line capacitance C_0 for microstrip circuitry are:

$$Z_0 = \frac{87}{\sqrt{\epsilon_r + 1.41}} ln \frac{5.98d}{0.8W + t} \quad \text{in Ohms} \tag{2.1.18}$$

$$T_{pd} = \frac{\sqrt{\epsilon_r}}{c} \quad \text{in psec/inch} \tag{2.1.19}$$

$$C_0 = \frac{T_{pd}}{Z_0} \quad \text{in pF/inch} \tag{2.1.20}$$

for $\frac{W}{d} < 1$

where:
c = speed of light in vacuum ($3.0x10^8$ m/s).
d = dielectric thickness, inches.
W = line width, inches.
t = line thickness, inches.
ϵ_r = relative permittivity (dielectric constant) of substrate.

The radiated electromagnetic interference (EMI) signals from the transmission lines will be a function of the line impedance, the length of the signal line, and the incident waveform characteristics. Interference between adjacent transmission lines, will depend directly on spacing, the distance to the reference planes, the length of parallelism between transmission lines, and signal rise time (IPC, 2003).

2.2 CSO Receiver Characteristics

2.2.1 DSB Configuration Receiver

The DSB configuration, implemented in the CSO receiver, allows a simpler design of the circuitry. In this case, the frequency response produces a superposition of the lower side band (LSB) and the upper side band (USB), these are the frequency bands of the RF signal selected by the mixer, obtaining at the receiver output

both signals simultaneously. This superposition increases the noise level of the IF output signal, as can be seen graphically in figure 2.2.1. To compensate for this rise in the noise level, it is necessary to increase the observation time of the telescope. Also, it can lead to line confusion, a phenomenon that occurs due to the difficulty of identifying if the signal comes from the LSB or the USB. The advantage of using this architecture is the lesser number of components used in the hardware, reducing the complexity in implementation (Rodriguez, 2015).

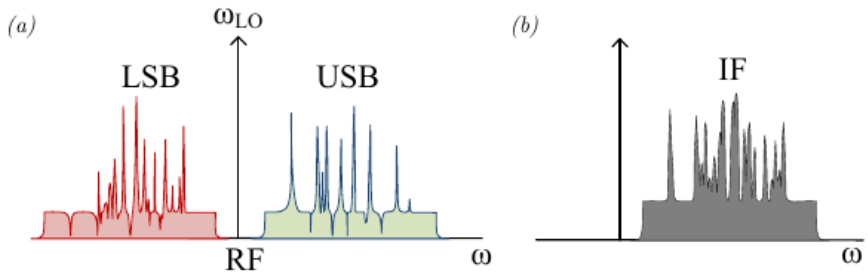

Figure 2.2.1: DSB configuration results, it can be seen the noise level of the IF signal increases concerning the RF signal components (Rodriguez, 2015).

2.2.2 The Status of the Current Receiver

The LCT will use the receiver initially designed for the CSO observatory, whose objective was to measure the 180 - 720 GHz spectral window with two receivers: one operating at 230 - 460 GHz and the other at 345 - 650 GHz. Figure 2.2.2 illustrates the spectral window covered by these two receivers. The objective of this thesis is to redesign the receiver covering the 230 - 460 GHz spectral band, shown in figure 2.2.3, while the second receiver will be developed at Normal Shanghai University. The 230 - 460 GHz receiver began its operations in 2012 at the CSO and continued until the observatory was decommissioned in 2015 (Golwala, 2023).

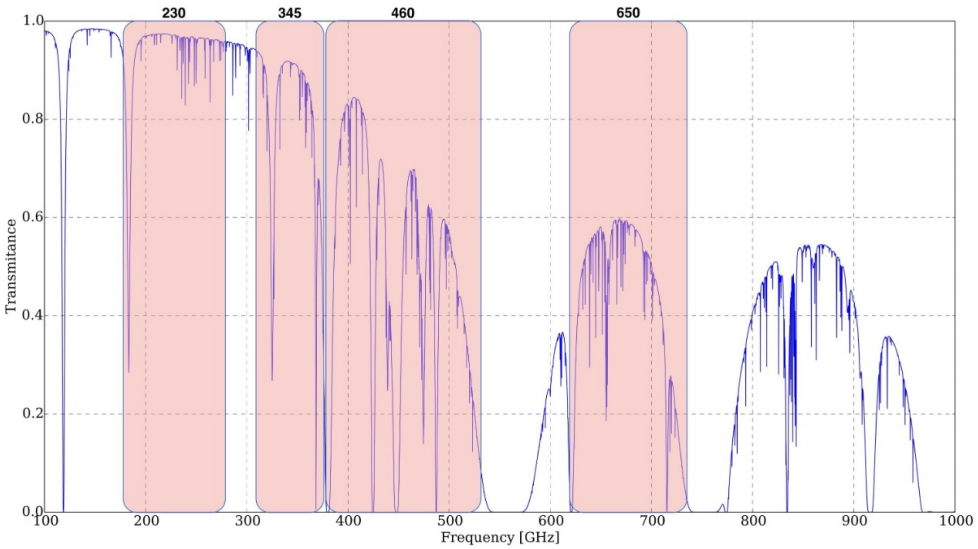

Figure 2.2.2: CSO spectral observation bands and atmospheric transmissibility at Mauna Kea as a function of the frequency (Golwala, 2023).

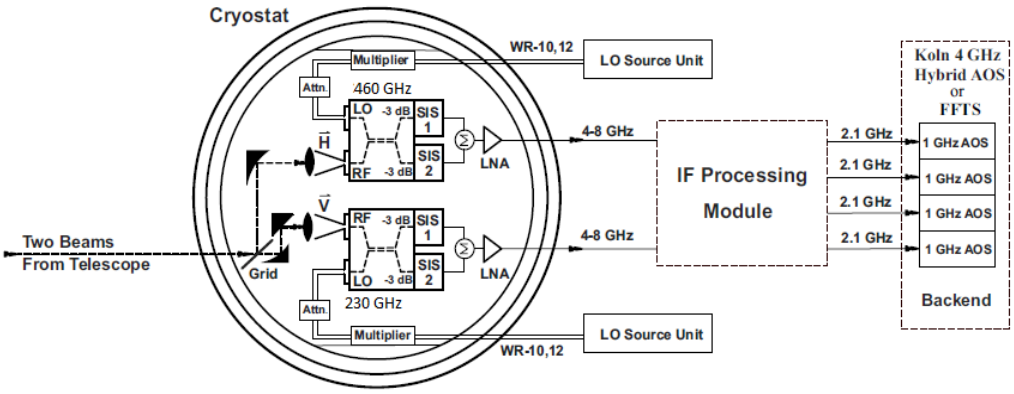

Figure 2.2.3: CSO receiver. It includes the cryostat containing the 230 and the 460 GHz of central frequency blocks. The RF signal enters the blocks where is downconverted to an IF signal, that is amplified in the LNA. At the output of the cryostat, the signal with a bandwidth that spans from 4 to 8 GHz, passes to the IF processing module, and finally to the digital Back-end (Kooi, 2008).

The original receiver front-end features a DSB architecture as illustrated in figure 2.2.3. As previously mentioned, this design has the disadvantage of generating a superposition of the sidebands LSB and USB, resulting in a higher noise level in the IF signal compared to the 2SB configuration. Figure 2.2.5 shows the original design of the IF circuit mounted on the module of the receiver. It shows the position of the 90° hybrid, which receives the RF and the LO signals. These signals are directed to the two SiS mixers, which are fed by the bias circuitry. Subsequently, the IF signals from both mixers enter the IF circuit board, where

they are filtered and combined in the Wilkinson summing node before finally exiting through the IF output.

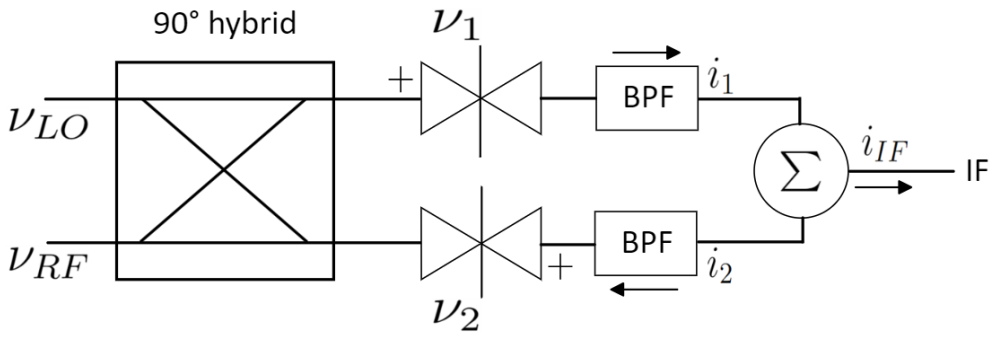

Figure 2.2.4: Current receiver schematic consists of several components. It begins with the 90° hybrid, followed by the mixers, then the bandpass filters, with the Wilkinson summing node as the final component (Kooi et al., 2014).

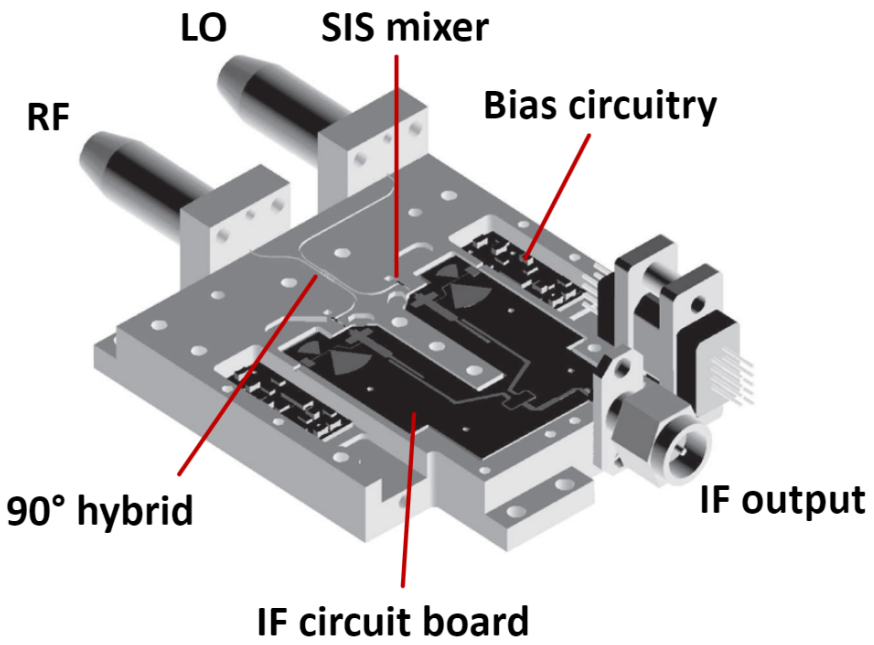

Figure 2.2.5: Original design of the IF circuit board, utilized in the CSO, mounted in the module's chassis (Kooi, 2008).

Kooi et al. (2014) conducted measurements of the receiver in the 230 GHz band to determine the receiver's optimal sensitivity as a function of the LO frequency. The receiver's noise temperature varies from 55 K at 185 GHz, 33 K at 246 GHz, to 51 K at 280 GHz, while the mixer exhibits a gain of 0 ± 1.5 dB. The results are illustrated in figure 2.2.6.

There are also measurements in the 460 GHz band. In this range, the noise

temperature varies from 32 K in 400 GHz, 34 K in 460 GHz, to 61 K in 520 GHz. In this scenario, the mixer exhibits a gain of 1 ± 1 dB, and the noise temperature of the mixer is 10% over the quantum limit. The measurement results are displayed in Figure 2.2.7.

Both results indicate that this receiver has a performance that is still considered state-of-the-art technology. This feature makes it suitable for spectral observations of complex astronomical signals, owing to its low contribution of noise to the resulting IF signal.

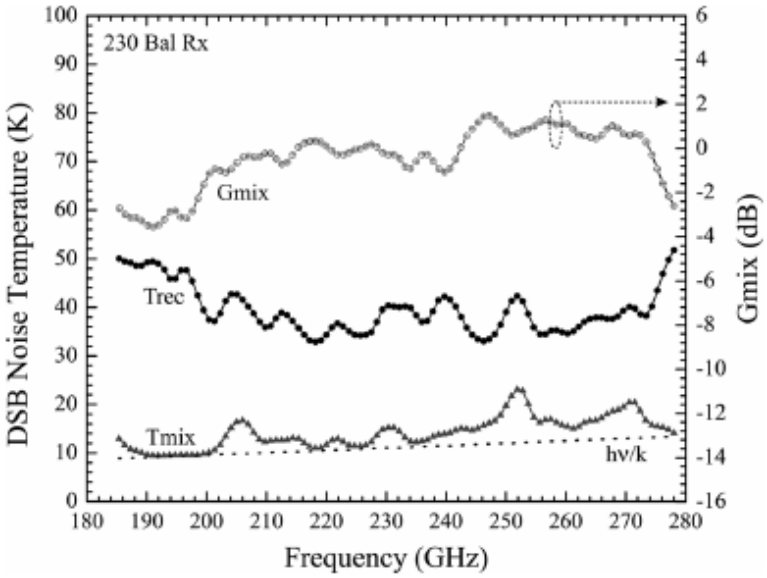

Figure 2.2.6: Receiver temperature (T_{rec}) in the 230 GHz band, mixer temperature (T_{mix}) and mixer gain (G_{mix}) as function of the LO frequency (Kooi et al., 2014).

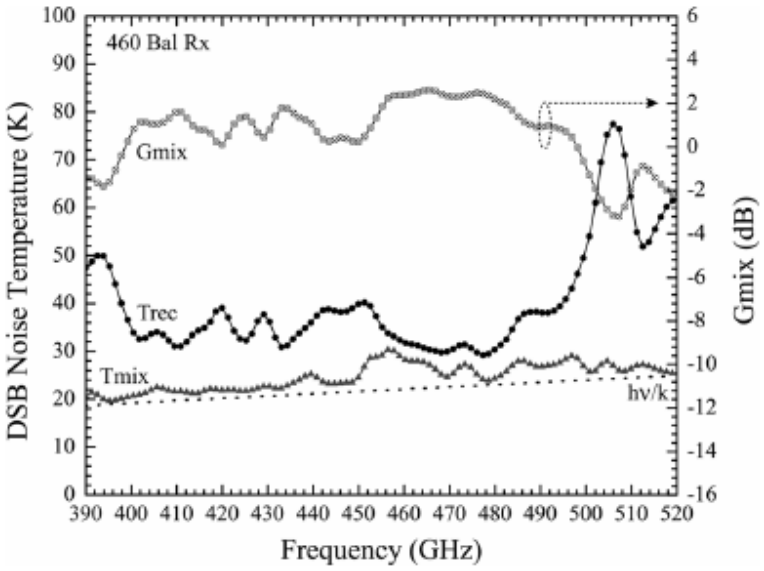

Figure 2.2.7: Receiver temperature (T_{rec}) in the 460 GHz band, mixer temperature (T_{mix}) and mixer gain (G_{mix}) as function of the LO frequency (Kooi et al., 2014).

2.2.3 Analytical model of the CSO Receiver.

In this section, the mathematical description of the current receiver performance was made to understand the characteristics of the circuit and the effect of each of its components over the RF and the IF signal. Figure 2.2.4 depicts the schematic of the existing receiver design. Notice the Wilkinson summing node at the output of the module, this node is intended to be removed to enable the independent retrieval of signals from each mixer.

The LCT circuit receiver currently utilizes a DSB (Double-Sideband) configuration. Both the RF and LO signals pass through a 90° hybrid, and the output of this component is split into two branches, differing in phase by $\phi = \pi/2$, with a phase error of $\Delta\phi$. Both signals are directed to the SIS mixers, where the product generated by this component undergoes filtration through a bandpass filter, effectively eliminating harmonics and the DC signal. Finally, the signals from both branches are combined at the Wilkinson summing node, resulting in an IF signal that encompasses the superposition of the sidebands.

2.2.3.1 90° Hybrid.

Referring to equations 2.1.10 and 2.1.11, we can derive the voltages at the hybrid output:

$$V_1 = \frac{1}{\sqrt{2}}(jV_{lo} + V_{rf}) \tag{2.2.1}$$

$$V_2 = \frac{1}{\sqrt{2}}(V_{lo} + jV_{rf}) \tag{2.2.2}$$

defining $V_{lo}(t) = V_{lo} \cdot cos(w_{lo}t + \theta_{lo})$ y $V_{rf}(t) = V_{rf} \cdot cos(w_{rf}t + \theta_{rf})$ we have finally:

$$V_1 = \frac{1}{\sqrt{2}}[V_{lo} \cdot cos(w_{lo}t + (\phi + \Delta\phi) + \theta_{lo}) + V_{rf} \cdot cos(w_{rf}t + \theta_{rf})] \tag{2.2.3}$$

$$V_2 = \frac{1}{\sqrt{2}}[V_{lo} \cdot cos(w_{lo}t + \theta_{lo}) + V_{rf} \cdot cos(w_{rf}t + (\phi + \Delta\phi) + \theta_{rf})] \tag{2.2.4}$$

With a phase change of $\phi = \frac{\pi}{2}$ introduced by the hybrid, θ represents the phases of the LO and RF signals, while $\Delta\phi$ signifies the phase error between branches. This latter term serves as a mathematical representation of any disparities that could exist in the actual implementation of the two circuit components.

2.2.3.2 SIS mixer.

Next, let's consider the mixer. We can represent the current through this component using a Taylor series:

$$i_1(t) = \sum_{n=0}^{\infty} \frac{K_n V_1(t)^n}{n!} \tag{2.2.5}$$

Since we have two mixers, with the second having $V_2(t) = -V_1(t)$, in this case, the current is represented as follows:

$$i_2(t) = \sum_{n=0}^{\infty} (-1)^n \frac{K_n V_2(t)^n}{n!} \tag{2.2.6}$$

Using K_n to denote the mixer gains, when we substitute 2.2.3 into 2.2.5 and 2.2.4

into 2.2.6 the resulting currents are:

$$\begin{aligned} i_1(t) = K_0 &+ \frac{K_1}{\sqrt{2}}[V_{lo} \cdot cos(w_{lo}t + (\phi + \Delta\phi) + \theta_{lo}) + V_{rf} \cdot cos(w_{rf}t + \theta_{rf})] \\ &+ \frac{K_2}{4}[V_{lo}^2 \cdot cos^2(w_{lo}t + (\phi + \Delta\phi) + \theta_{lo}) \\ &+ 2V_{lo} \cdot cos(w_{lo}t + (\phi + \Delta\phi) + \theta_{lo})V_{rf} \cdot cos(w_{rf}t + \theta_{rf}) \\ &+ V_{rf}^2 \cdot cos^2(w_{rf}t + \theta_{rf})] \\ &+ \frac{K_3}{6\sqrt{2}^3}[V_{lo}^3 \cdot cos^3(w_{lo}t + (\phi + \Delta\phi) + \theta_{lo}) \\ &+ 3V_{lo}^2 \cdot cos^2(w_{lo}t + (\phi + \Delta\phi) + \theta_{lo})V_{rf} \cdot cos(w_{rf}t + \theta_{rf}) \\ &+ 3V_{lo} \cdot cos(w_{lo}t + (\phi + \Delta\phi) + \theta_{lo})V_{rf}^2 \cdot cos^2(w_{rf}t + \theta_{rf}) \\ &+ V_{rf}^3 \cdot cos^3(w_{rf}t + \theta_{rf})] \end{aligned} \tag{2.2.7}$$

Similarly, we can derive the current i_2:

$$\begin{aligned} i_2(t) = K_0 &- \frac{K_1}{\sqrt{2}}[V_{lo} \cdot cos(w_{lo}t + \theta_{lo}) + V_{rf} \cdot cos(w_{rf}t + (\phi + \Delta\phi) + \theta_{rf})] \\ &+ \frac{K_2}{4}[V_{lo}^2 \cdot cos^2(w_{lo}t + \theta_{lo}) \\ &+ 2V_{lo} \cdot cos(w_{lo}t + \theta_{lo})V_{rf} \cdot cos(w_{rf}t + (\phi + \Delta\phi) + \theta_{rf}) \\ &+ V_{rf}^2 \cdot cos^2(w_{rf}t + (\phi + \Delta\phi) + \theta_{rf})] \\ &- \frac{K_3}{6\sqrt{2}^3}[V_{lo}^3 \cdot cos^3(w_{lo}t + \theta_{lo}) \\ &+ 3V_{lo}^2 \cdot cos^2(w_{lo}t + \theta_{lo})V_{rf} \cdot cos(w_{rf}t + (\phi + \Delta\phi) + \theta_{rf}) \\ &+ 3V_{lo} \cdot cos(w_{lo}t + \theta_{lo})V_{rf}^2 \cdot cos^2(w_{rf}t + (\phi + \Delta\phi) + \theta_{rf}) \\ &+ V_{rf}^3 \cdot cos^3(w_{rf}t + (\phi + \Delta\phi) + \theta_{rf})] \end{aligned} \tag{2.2.8}$$

Now, we will consider only the quadratic part of equations 2.2.7 and 2.2.8, as it contains the sum and subtraction of the LO and RF signals.

$$\begin{aligned} i(t) = \frac{K}{4}&[V_{lo}^2 \cdot cos^2(w_{lo}t + (\phi + \Delta\phi) + \theta_{lo}) \\ &+ 2V_{lo} \cdot cos(w_{lo}t + (\phi + \Delta\phi) + \theta_{lo})V_{rf} \cdot cos(w_{rf}t + \theta_{rf}) \\ &+ V_{rf}^2 \cdot cos^2(w_{rf}t + \theta_{rf})] \end{aligned}$$

using $cos^2(x) = \frac{1+cos(2x)}{2}$,

$$i(t) = \frac{K}{4}[\frac{1}{2}V_{lo}^2 + \frac{1}{2}V_{lo}^2 cos(2w_{lo}t + 2(\phi + \Delta\phi) + 2\theta_{lo}) + \frac{1}{2}V_{rf}^2 + \frac{1}{2}V_{rf}^2 cos(2w_{rf}t + 2\theta_{lo}) + 2V_{lo}V_{rf} \cdot cos(w_{lo}t + (\phi + \Delta\phi) + \theta_{lo}) \cdot cos(w_{rf}t + \theta_{rf})]$$

$$i(t) = \frac{K}{4}[\frac{1}{2}(V_{lo}^2 + V_{rf}^2) + \frac{1}{2}V_{lo}^2 cos(2w_{lo}t + 2(\phi + \Delta\phi) + 2\theta_{lo}) + \frac{1}{2}V_{rf}^2 cos(2w_{rf}t + 2\theta_{rf}) + 2V_{lo}V_{rf} \cdot cos(w_{lo}t + (\phi + \Delta\phi) + \theta_{lo}) \cdot cos(w_{rf}t + \theta_{lrf})]$$

Using the identity $cos(x) \cdot cos(y) = \frac{1}{2}[cos(x+y) + cos(x-y)]$,

$$i(t) = \frac{K}{4}[\frac{1}{2}(V_{lo}^2 + V_{rf}^2) + \frac{1}{2}V_{lo}^2 cos(2w_{lo}t + 2(\phi + \Delta\phi) + 2\theta_{lo}) + \frac{1}{2}V_{rf}^2 cos(2w_{rf}t + 2\theta_{rf}) + V_{lo}V_{rf}(cos(w_{lo}t + (\phi + \Delta\phi) + w_{rf}t + \theta_{lo} + \theta_{rf}) + cos(w_{lo}t + (\phi + \Delta\phi) - w_{rf}t + \theta_{lo} - \theta_{rf}))]$$

$$i(t) = \frac{K}{4}[\frac{1}{2}(V_{lo}^2 + V_{rf}^2) + \frac{1}{2}V_{lo}^2 cos(2w_{lo}t + 2(\phi + \Delta\phi) + 2\theta_{lo}) + \frac{1}{2}V_{rf}^2 cos(2w_{rf}t + 2\theta_{rf}). + V_{lo}V_{rf}cos(w_{lo}t + w_{rf}t + (\phi + \Delta\phi) + \theta_{lo} + \theta_{rf}) + V_{lo}V_{rf}cos(w_{lo}t - w_{rf}t + (\phi + \Delta\phi) + \theta_{lo} - \theta_{rf})]$$

Now, we can decompose the signal that will pass through the filters.

2.2.3.3 Filter

As mentioned earlier, by applying trigonometric identities to the currents obtained from the mixer, we obtain:

$$i_{1f} = KV_{lo} \cdot cos(w_{lo}t + (\phi + \Delta\phi) + \theta_{lo})V_{rf} \cdot cos(w_{rf}t + \theta_{rf}) \tag{2.2.9}$$

$$i_{2f} = KV_{lo} \cdot cos(w_{lo}t + \theta_{lo})V_{rf} \cdot cos(w_{rf}t + (\phi + \Delta\phi) + \theta_{rf}) \tag{2.2.10}$$

With i_{1f} and i_{2f} the filtered signals.

The previous results consider all the following signals:

$$
\begin{aligned}
i(t) = \frac{K}{4}[&\frac{1}{2}(V_{lo}^2 + V_{rf}^2) \quad \text{DC component} \\
&+ \frac{1}{2}V_{lo}^2 cos(2w_{lo}t + 2(\phi + \Delta\phi) + 2\theta_{lo}) \quad \text{LO signal second harmonic} \\
&+ \frac{1}{2}V_{rf}^2 cos(2w_{rf}t + 2\theta_{rf}) \quad \text{RF signal second harmonic} \\
&+ V_{lo}V_{rf} cos(w_{lo}t + w_{rf}t + (\phi + \Delta\phi) + \theta_{lo} + \theta_{rf}) \quad \text{sum of frequencies} \\
&+ V_{lo}V_{rf} cos(w_{lo}t - w_{rf}t + (\phi + \Delta\phi) + \theta_{lo} - \theta_{rf})] \quad \text{subtraction of frecuencies}
\end{aligned}
$$

The bandpass filter effectively suppresses the DC component and the harmonics, allowing only the frequency subtraction to pass through.

2.2.3.4 The Wilkinson Summing Node

The final component is the addition of the signals of the two branches. We can describe the effect of the summation node by adding the output currents of equations 2.2.9 and 2.2.10 as follows:

$$
\begin{aligned}
i_{if} &= i_{1f}(t) - i_{2f}(t) \\
&= KV_{lo} \cdot cos(w_{lo}t + (\phi + \Delta\phi) + \theta_{lo})V_{rf} \cdot cos(w_{rf}t + \theta_{rf}) \\
&\quad - KV_{lo} \cdot cos(w_{lo}t + \theta_{lo})V_{rf} \cdot cos(w_{rf}t + (\phi + \Delta\phi) + \theta_{rf}) \\
&= KV_{lo}V_{rf}[cos(w_{lo}t + (\phi + \Delta\phi) + \theta_{lo}) \cdot cos(w_{rf}t + \theta_{rf}) \\
&\quad - cos(w_{lo}t + \theta_{lo}) \cdot cos(w_{rf}t + (\phi + \Delta\phi) + \theta_{rf})]
\end{aligned}
$$

In this design, the selected component is a 90° hybrid, so we know that $\phi = \frac{\pi}{2}$. Using the trigonometric identity $cos(x + \frac{\pi}{2}) = -sin(x)$ it simplifies to:

$$i_{if} = KV_{lo}V_{rf}[-sin(w_{lo}t+\Delta\phi+\theta_{lo})\cdot cos(w_{rf}t+\theta_{rf})+cos(w_{lo}t+\theta_{lo})\cdot sin(w_{rf}t+\Delta\phi+\theta_{rf})]$$

Applying trigonometric identity corresponds to:

$$i_{if} = KV_{lo}V_{rf}[sin((w_{rf} - w_{lo})t + \Delta\phi + \theta_{lo} - \theta_{rf})]$$

For simplification, we can consider the incoming signal phases as $\theta_{lo} = \frac{\pi}{2}$ and $\theta_{rf} = 0$ (Kooi, 2008), the resulting IF signal at the summing node output is:

$$i_{if} = KV_{lo}V_{rf}[cos(w_{if}t + \Delta\phi)] \tag{2.2.11}$$

While this balanced mixer architecture represents a significant technological advancement, it does have certain limitations. As a DSB system, we end up with an IF signal that is influenced by noise resulting from the overlap of the signal of interest and image signal as the final product.

2.3 Sideband Separating (2SB) Receiver Characteristics

2.3.1 2SB Configuration Receiver

In this thesis, we propose to evaluate the feasibility of implementing the 2SB configuration in the first light of the LCT. In the 2SB architecture case is possible to observe in two sidebands simultaneously independently, reducing the noise in each band by a factor of two, and increasing the bandwidth of the observations. The 2SB configuration has the inconvenience that the sideband rejection depends highly on the amplitude and phase imbalance of the entire system. To reduce the imbalance, the total electric length and gain have to be the same in both branches of the system. The mixers used in this design should have equal efficiency, and the hybrids and power dividers should perform very close to their nominal design. It is very difficult to achieve this performance in reality for large RF and IF bandwidth (Rodriguez, 2015). In summary, in the 2SB configuration, the RF signal can be separated into two outputs, avoiding sideband superposition and reducing noise in the IF signal, as seen in figure 2.3.1. The main disadvantage of this architecture is the great number of components, making it a more complex system.

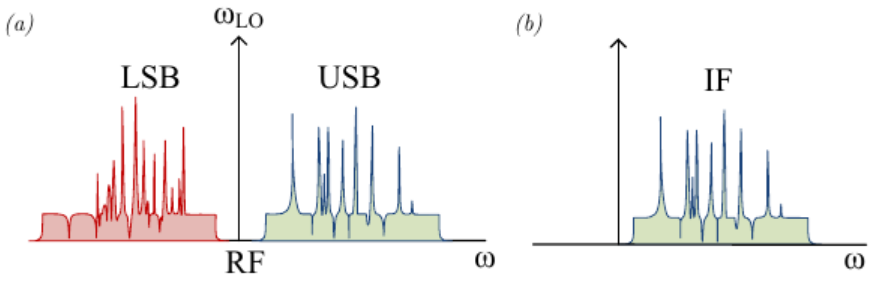

Figure 2.3.1: 2SB configuration performance, in the IF output signal the upper side band has been selected (Rodriguez, 2015).

2.3.2 2SB Mathematical Analysis

The mathematical analysis of the 2SB configuration was made to show the performance of this kind of circuit and the effect on the IF signal at the output. The analysis presented here pertains to a typical sideband separation circuit. Euler notation was employed to depict the signal pathway across various mixer components. This model serves as a reference for the subsequent evaluation of different configurations tested in this study, with the aim of identifying the configuration that allows the 2SB requirement.

Figure 2.3.2 shows a standard 2SB mixer configuration, which consists of two mixers and two necessary hybrids for this architecture, one in the RF stage and the other in the IF stage. In this case, both hybrids produce a 90° phase shift between the two output ports. The LO signal passes through a splitter and feeds both mixers in phase. The general schematic of the sideband separation (2SB) design is presented, followed by a theoretical explanation of the circuit's behavior to demonstrate its performance. The IF filters has been omitted for simplicity.

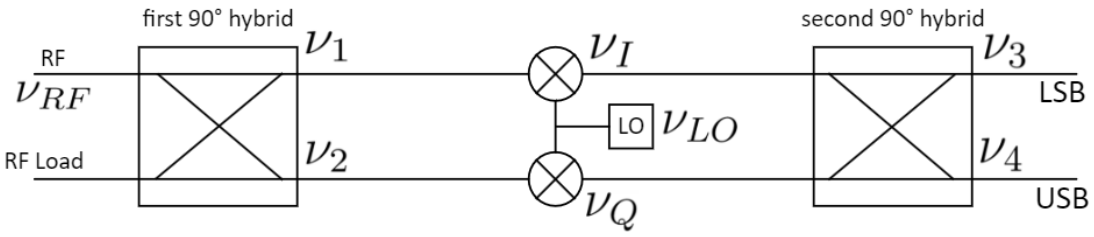

Figure 2.3.2: General sideband separation architecture.

If we define the RF and LO signals as follows:

$\nu_{RF} = V_{RF}^{U} e^{-i(w_{RF}^{U} t)} + V_{RF}^{L} e^{-i(w_{RF}^{L} t)}$

$\nu_{LO} = V_{LO} e^{i(w_{LO} t)}$

Here, V_{RF}^{U} is the amplitude of the signal in the upper sideband, while V_{RF}^{L} corresponds to the amplitude of the signal in the lower sideband. The first component is a 90° hybrid, here we have at the outputs:

$\nu_1 = \nu_{RF}^{U} + \nu_{RF}^{L}$
$\nu_2 = \nu_{RF}^{U} \cdot j + \nu_{RF}^{L} \cdot j$

Where $j = e^{-i(\frac{\pi}{2})}$, then we have:

$$\nu_1 = V_{RF}^{U} e^{-i(w_{RF}^{U} t)} + V_{RF}^{L} e^{-i(w_{RF}^{L} t)}$$

$$\nu_2 = V_{RF}^{U} e^{-i(w_{RF}^{U} t - \frac{\pi}{2})} + V_{RF}^{L} e^{-i(w_{RF}^{L} t - \frac{\pi}{2})}$$

Now in the mixer, we have the following:
For ν_I:

$$\nu_I = [V_{RF}^{U} e^{-i(w_{RF}^{U} t)} + V_{RF}^{L} e^{-i(w_{RF}^{L} t)}] V_{LO} e^{i(w_{LO} t)}$$

$$\nu_I = V_{LO} V_{RF}^{U} e^{-i(w_{RF}^{U} t) + i(w_{LO} t)} + V_{LO} V_{RF}^{L} e^{-i(w_{RF}^{L} t) + i(w_{LO} t)}$$

$$\nu_I = V^{U} e^{-i(w_{RF}^{U} t - w_{LO} t)} + V^{L} e^{-i(w_{RF}^{L} t - w_{LO} t)}$$

$$\nu_I = V^{U} e^{-i(w_{IF}^{U} t)} + V^{L} e^{-i(-w_{IF}^{L} t)}$$

$$\nu_I = V^{U} e^{-i(w_{IF}^{U} t)} + V^{L} e^{i(w_{IF}^{L} t)}$$

For ν_Q:

$$\nu_Q = [V_{RF}^{U} e^{-i(w_{RF}^{U} t - \frac{\pi}{2})} + V_{RF}^{L} e^{-i(w_{RF}^{L} t - \frac{\pi}{2})}] V_{LO} e^{i(w_{LO} t)}$$

$$\nu_Q = V_{LO} V_{RF}^{U} e^{-i(w_{RF}^{U} t - \frac{\pi}{2}) + i(w_{LO} t)} + V_{LO} V_{RF}^{L} e^{-i(w_{RF}^{L} t - \frac{\pi}{2}) + i(w_{LO} t)}$$

$$\nu_Q = V^{U} e^{-i(w_{RF}^{U} t - w_{LO} t - \frac{\pi}{2})} + V^{L} e^{-i(w_{RF}^{L} t - w_{LO} t - \frac{\pi}{2})}$$

$$\nu_Q = -V^{U} e^{-i(w_{IF}^{U} t - \frac{\pi}{2})} - V^{L} e^{-i(-w_{IF}^{L} t - \frac{\pi}{2})}$$

$$\nu_Q = -V^{U} e^{-i(w_{IF}^{U} t - \frac{\pi}{2})} - V^{L} e^{i(w_{IF}^{L} t + \frac{\pi}{2})}$$

For the second hybrid, we have the outputs defined as:

$\nu_3 = \nu_I + \nu_Q \cdot j$
$\nu_4 = \nu_I \cdot j + \nu_Q$

With $j = e^{-i(\frac{\pi}{2})}$, so we have:
For ν_3:

$$\nu_3 = V^U e^{-i(w_{IF}^U t)} + V^L e^{-i(w_{IF}^L t)} + V^U e^{-i(w_{IF}^U t - \pi)} + V^L e^{-i(w_{IF}^L t)}$$

$$\nu_3 = V^U e^{-i(w_{IF}^U t)} + V^L e^{-i(w_{IF}^L t)} - V^U e^{-i(w_{IF}^U t)} + V^L e^{-i(w_{IF}^L t)}$$

$$\nu_3 = V^L e^{-i(w_{IF}^L t)} + V^L e^{-i(w_{IF}^L t)}$$

$$\nu_3 = 2V^L e^{-i(w_{IF}^L t)} \quad \text{(LSB)} \tag{2.3.1}$$

For ν_4:

$$\nu_4 = V^U e^{-i(w_{IF}^U t - \frac{\pi}{2})} + V^L e^{-i(w_{IF}^L t + \frac{\pi}{2})} + V^U e^{-i(w_{IF}^U t - \frac{\pi}{2})} + V^L e^{-i(w_{IF}^L t - \frac{\pi}{2})}$$

$$\nu_4 = V^U e^{-i(w_{IF}^U t - \frac{\pi}{2})} + V^L e^{-i(w_{IF}^L t + \frac{\pi}{2})} + V^U e^{-i(w_{IF}^U t - \frac{\pi}{2})} - V^L e^{-i(w_{IF}^L t + \frac{\pi}{2})}$$

$$\nu_4 = V^U e^{-i(w_{IF}^U t - \frac{\pi}{2})} + V^U e^{-i(w_{IF}^U t - \frac{\pi}{2})}$$

$$\nu_4 = 2V^U e^{-i(w_{IF}^U t)} \quad \text{(USB)} \tag{2.3.2}$$

As evident from equations 2.3.1 and 2.3.2, the separation of the sidebands has been achieved, and the sidebands are present at each output of the second hybrid.

2.3.3 Superconductor-Insulator-Superconductor (SIS) Mixer

An SIS junction consists of two superconductor layers with a very thin layer of insulator between them. The charge carriers in the SIS tunnel junctions have discrete energy levels and can tunnel through the barrier in a quantum mechanical way. Josephson mixers are heterodyne mixers that use Cooper pair tunneling, while SIS mixers are heterodyne mixers that use single particle tunneling (Kooi, 2008). SIS mixers are widely used in radio astronomy for millimeter spectroscopy, as they are installed on many radio telescopes around the world.

The energy gap between the occupied and unoccupied states in SIS junctions is about $\approx 1\ mV$, which is similar to the photon energies at 300 GHz. In addition,

the local oscillator power requirements are ≈ 1000 times lower than are needed for conventional mixers. The design of these devices is simpler, as they are planar devices that are made on a substrate using lithography. In real SISs, the insulator is usually 0.6 to 1 nm thick to achieve high current densities (Wengler, 1992).

Referred to the image 2.3.3, when the SIS junction is biased to a value of $2\Delta/e$, the filled states on the left side reach the level of the unfilled band shown on the right, and the electrons can quantum mechanically tunnel through the insulating strip. In the $I - V$ curve for an SIS device, the sudden jumps are typical of quantum-mechanical phenomena.

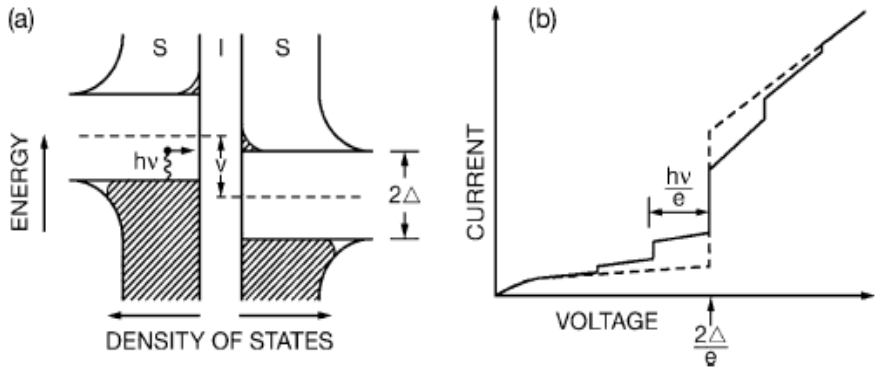

Figure 2.3.3: (a) A sketch of the energy bands of an SIS layer, the gap between the filled state (shaded) and the empty states is $2\Delta/e$. (b) The $I - V$ curve of the SIS junction. The dashed line is the behavior without LO power, the solid line is the behavior with LO power. When DC biased the SIS mixer converts photons to a lower frequency (Wilson et al., 2008).

In SIS mixers, Cooper pairs are not useful, as they cause Josephson currents in the superconductor (Wengler, 1992). This increases the noise in an SIS mixer, so they need to be eliminated. In addition to the mixer DC bias and LO signal, at frequencies above 120 GHz, one must apply a steady magnetic field to eliminate the Josephson effect. In figure 2.3.4, we can see two electro-magnets mounted on top of the mixer block of the current LCT receiver. The Josephson noise in the SIS tunnel junctions may be individually suppressed by these components.

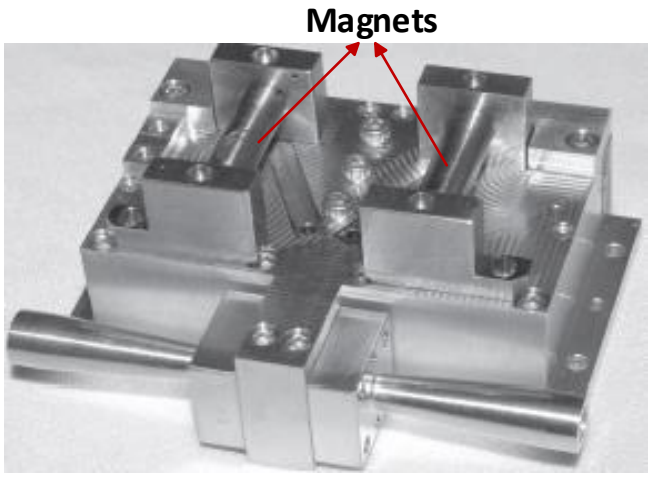

Figure 2.3.4: The physical mixer block of the current receiver with two electro magnets mounted on top (Kooi, 2008).

2.3.4 Lumped Elements for Microwave Integrated Citcuits

Lumped elements such as resistors, capacitors, and inductors can be implemented at microwave frequencies if the length of the component is very small in comparison with the operating wavelength. Usually, the characteristics of these elements are far from ideal, generating undesirable effects such as parasitic capacitance and/or inductance, spurious resonances, fringing fields, loss, and differences in phase between the input and output signals. In figure 2.3.5, a collection of examples showcasing the fabrication of these components is presented.

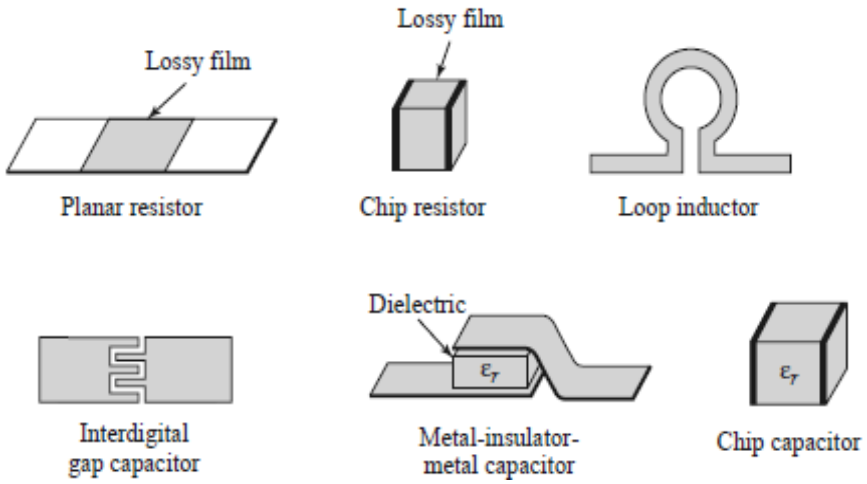

Figure 2.3.5: Examples of the type of fabrication of lumped elements used in microwave integrated circuits (Pozar, 2011).

Thin films of lossy material such as nichrome, or dropped semiconductor material, are used to make resistors. In monolithic circuits, these films can be grown or deposited, while in hybrid circuits, chip resistors made from a lossy film on a ceramic chip can be soldered or bonded.

A short length or loop of transmission line can be used to make small inductance values, and a spiral inductor can make larger values (about 10 nH). Larger inductance values usually have more loss and more shunt capacitance, which causes a resonance that limits the maximum operating frequency.

There are several methods to make capacitors. A shunt capacitance in the range of 0-0.1 pF can be provided by a short stub of transmission line. A series capacitance of up to about 0.5 pF can be provided by a single gap, or a set of interdigital gaps, in a transmission line. Larger values (up to about 25 pF) can be made using metal-insulator-metal junctions in either monolithic or chip form (Pozar, 2011).

Chapter 3

Tools and Requirements for the Development of the LCT Receiver

This chapter will outline the requirements and tools employed in this study. Simulations play a pivotal role in this research as they enable the development of experiments with the IF circuit board. They provide us with the capability to introduce components with specific characteristics on the circuit and promptly obtain results, with the option to make model adjustments on the fly.

The mathematical analysis of the original circuit enables us to discern the signal's behavior as it traverses specific components. This insight aids in comprehending the steps required to establish a 2SB configuration in the new design. The feasibility of this scenario has also been examined through mathematical analysis, illustrating the process of implementing this configuration in the new IF circuit board design.

3.1 The Wilkinson Summing Node and The CSO IF Circuit

The Wilkinson Divider is used to divide and combine signals, maintaining their phase. The Wilkinson will split a signal into two signals with 0 phase shift between them. The Wilkinson divider achieves excellent isolation through the use of quarter-wavelength transmission lines and a balance resistor between the inputs/outputs. It is particularly simple and can easily be realized using printed

components on a printed circuit board. It is also possible to use lumped elements.

Figure 3.1.1 shows a Wilkinson power divider/combiner scheme, the resistor between the two output ports enables the two outputs to match while also providing isolation. In order to see how the Wilkinson divider works, consider a signal entering port 1, the signal reaches the physical split and passes to both outputs, ports 2 and 3. As the power is being split, it is necessary to ensure that the impedances within the Wilkinson divider are maintained. To achieve this, the two output ports of $2Z_0$ in parallel will present an overall impedance of Z_0. The impedance transformation is achieved by placing a quarter wave transmission line between the star point and the output. The transmission line has an impedance of $Z_{match} = \sqrt{2}Z_0$. In this way, the impedance within the system is maintained.

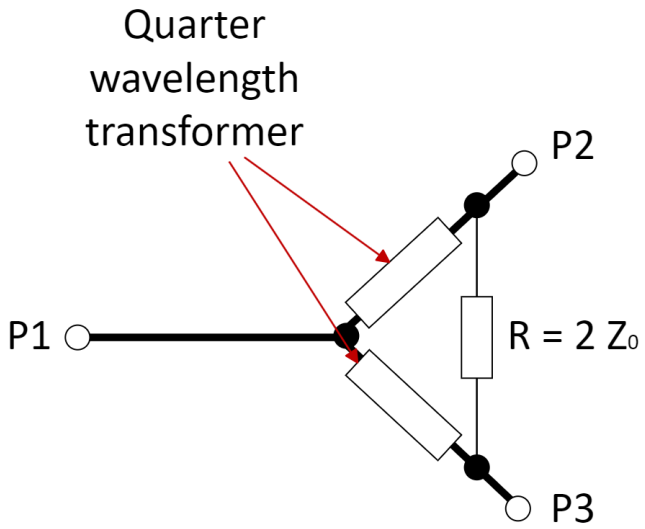

Figure 3.1.1: Wilkinson power divider/combiner scheme. Here $R = 2Z_0$ is the value of the terminating resistor connected between the two ports, with Z_0 the characteristic impedance of the system. The impedance of the quarter wave transformer in the legs of the power divider/combiner is $Z_{match} = \sqrt{2}Z_0$.

The Wilkinson power divider operates in both directions and can also be used as a combiner. In this mode signals entering ports 2 and 3 will emerge at port 1. Consider power entering port 2, it will split equally between the resistor and port 1. As the signal enters port 2, half passes through the resistor and the other half passes through the other quarter wave transformer. It appears at the star point, that any power passing through the other quarter wave transformer to port 3 will be out of phase with that appearing via the resistor as it will have passed through two quarter wave lines. As a result, there is isolation between the two ports, half the power is dissipated within the resistor and half appears at port 1.

The goal of this thesis is to create a new design for the IF circuit board of the LCT receiver. This modification will be based on the current circuit design. Figure 3.1.2 provides an image of the circuit board currently utilized in the CSO, along with a close-up of the Wilkinson summing node. This node combines the sidebands, generating a single output signal.

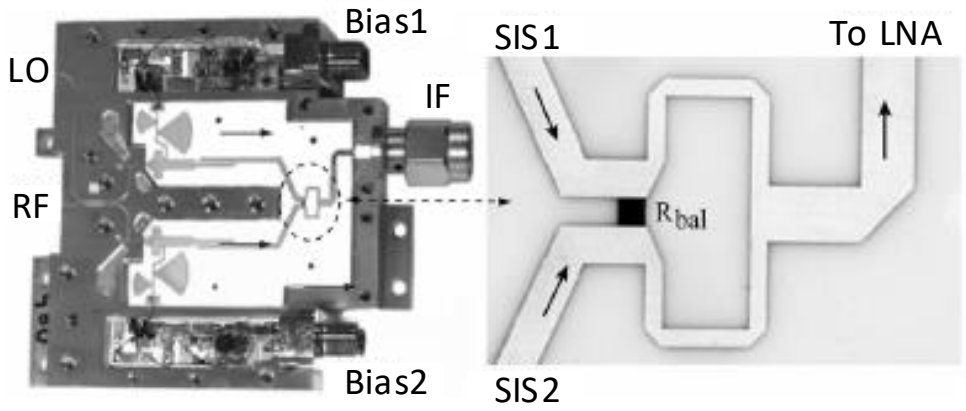

Figure 3.1.2: (Left) inside of the receiver block, the input of the RF and LO signals are on the left side, and the IF signal output is on the right side. (Right) Close up to the Wilkinson summing node (Kooi et al., 2014).

For the new design, the modification involves removing the Wilkinson summing node and generating two IF outputs. Additionally, another modification entails replacing the coupled lines filter and the radial stubs with passive components.

These modifications have some limitations. The transmission lines must undergo minimal alterations, because the circuit uses an SIS mixer that requires DC biasing through the same transmission lines. Moreover, the substrate board must keep the same dimensions, as it will be mounted on the same package. Lastly, to obtain the two IF outputs, the package must be modified to include a new IF output connector.

3.2 Necessary Software for Modeling and Simulation

3.2.1 Design on ANSYS HFSS

To construct the circuit model and conduct simulations to verify its performance, we must employ reliable and precise software that enables us to work with accurate measurements and provide the results we need for evaluation.

To accomplish this task, we employed the High-Frequency Software Simulation (HFSS, ANSYS (2023)). This is a multipurpose, full wave 3D electromagnetic (EM) simulation software for designing and simulating high-frequency electronic products such as antennas, components, interconnects, connectors, ICs, and PCBs.

In this project, we utilize HFSS to construct a 3D model of the TDR and perform simulations until we achieve results consistent with Jacob Kooi's measurements and simulations of the TDR. Upon attaining these positive outcomes, we will employ HFSS to modify the IF circuit and develop the design for the new LCT IF circuit board. The new IF circuit model and the results from these HFSS simulations will constitute the final steps before the fabrication of the LCT receiver.

3.2.2 Design on Cadence AWR

To validate the simulation results, we require software that enables us to conduct quick simulations by adjusting specific component characteristics. Additionally, for visualizing the downloaded S parameters of a component (e.g., a capacitor), we need dependable RF software with the capability to generate plots efficiently.

The selected software for this task was Cadence AWR (Cadence Design Systems, 2023). The platform provides RF/microwave engineers with integrated high-frequency circuits, systems, electromagnetic simulation technologies, and electronic design automation to develop physically realizable electronics ready for manufacturing.

In this thesis, we utilize AWR to construct a model of the new LCT IF circuit board using data extracted from the results of HFSS simulations. Various passive components will be incorporated into the AWR model to assess their performance

in the IF circuit and compare them to identify the optimal component option.

3.3 Acquisition of the Passive Components' S-Parameters

To conduct simulations with the new design, we must incorporate the new components into the circuit model. One approach to achieve this is by downloading the S parameters of these components from the manufacturer's website. For this particular experiment, we required both a capacitor and a resistor. Hence, we searched for an 'S2P' file format, which is compatible with the HFSS software and enables us to integrate the files into the simulations.

Specifically, we chose the Skyworks SC06801518 capacitor, and we obtained its S parameters from Skyworks Solutions (2023). As for the resistor, we acquired its S parameters from a distributor's website, Mouser Electronics (2023), and the chosen component was the VISHAY CH0402FP330R. Further details regarding the application of these components are provided in the Results section.

3.4 Requirements for the Analytical Model of the Receiver

To mathematically illustrate the operation of the current circuit, the methodology employed for the calculations closely follows Pozar (2011). The RF and LO signals are expressed as trigonometric functions, and mathematical operations are applied to these signals as they traverse the various components of the circuit. In this regard, the calculations are presented sequentially, following the order of the components from the RF input (and LO input), to the 90° hybrid, the SIS mixer, the bandpass filter, the summing node, and ultimately to the IF output.

On the other hand, to provide a mathematical description of the sideband separation receiver, Euler's notation was employed. Furthermore, an investigation of the feasibility of porting this architecture to a 2SB receiver was conducted using the same notation. This approach enables us to expedite calculations and assess various scenarios involving the addition of different components to the circuit.

Lastly, every calculation comes with a schematic of the circuit, so each component

can be visualized easily. Also, a schematic was created to propose a new configuration for the receiver.

3.5 Chapter Closeout

The simulation methodology employed in this study was chosen to allow for modifications to the existing circuit without the need to alter the physical circuit itself. The software used enables us to achieve results that closely match measurements, as demonstrated by Kooi (2005), even when new components are introduced. Additionally, the S parameter file of these components is introduced in the simulations of HFSS and AWR.

The calculations conducted in this study using trigonometric functions aid in comprehending the circuit's performance. Additionally, employing Euler's notation to examine various scenarios in the circuit proposal facilitated our evaluation of the addition of several new components in the circuit.

Chapter 4

Results

In this chapter, simulations of the technology demonstration receiver (TDR) circuit of the CSO are presented. The TDR serves as a testing circuit to assess the performance of the IF circuit board. The objective is to replicate the results obtained in the original measurements and simulations, comprehensively understand the performance of each circuit component, and subsequently proceed with the modifications of the DSB circuit to increase the bandwidth of the IF signal.

Conversely, a mathematical analysis has been conducted to elucidate the current receiver's performance. Following this, an examination of the feasibility of implementing a 2SB architecture in the circuit board was undertaken. Finally, a novel receiver configuration that would overcome the current design limitations is provided.

4.1 Technology Demonstration Receiver (TDR): a model for the IF circuit.

To begin the simulations, we required a reference point that provides us with a design comparison. Kooi (2005) provides measurements and simulations of the Technology Demonstration Receiver (TDR), an instrument designed to evaluate the performance of the original circuit design as it accurately represents the entire circuit. Figure 4.1.1 displays an image of the TDR indicating the name of each port.

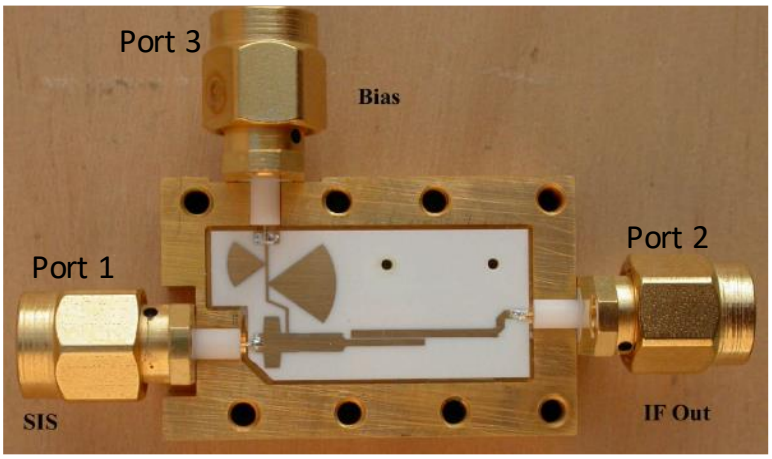

Figure 4.1.1: The test block for the TDR consists of three ports. The SIS port indicates the IF signal input, the Bias port is the SIS energization, and lastly, we have the IF output port (Kooi, 2005).

The comparison of the measurements and the simulations created by J. Kooi for the TDR are displayed in figures 4.1.2, 4.1.3, and 4.1.4. These scattering parameters, referred to as S parameters, will be utilized for comparing them with the simulations of this thesis's TDR design.

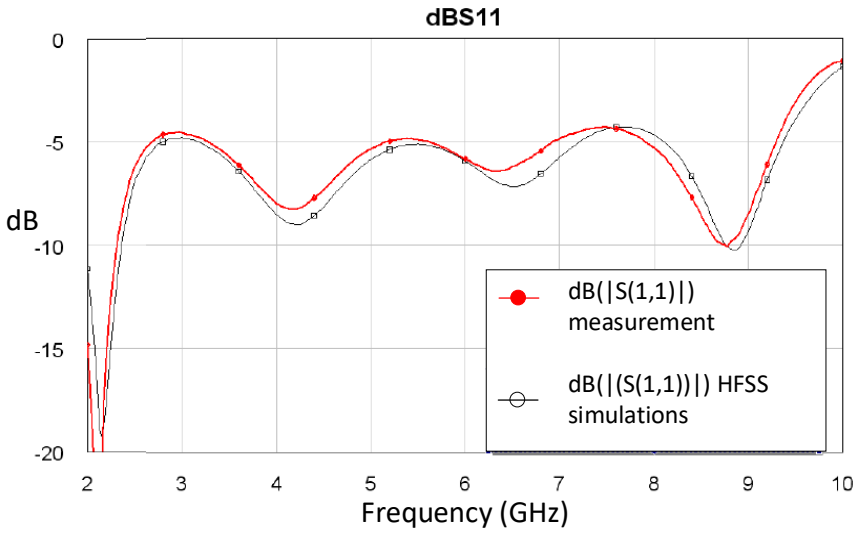

Figure 4.1.2: Signal reflection in port 1. The black line represents the simulations, while the red line denotes the measurements (Kooi, 2005).

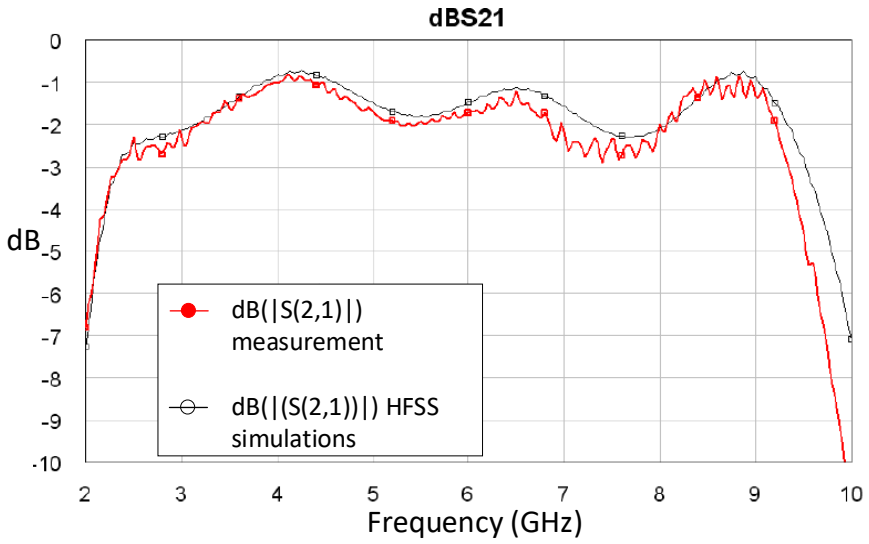

Figure 4.1.3: Signal transmission from port 1 to port 2. The black line represents the simulations, while the red line denotes the measurements (Kooi, 2005).

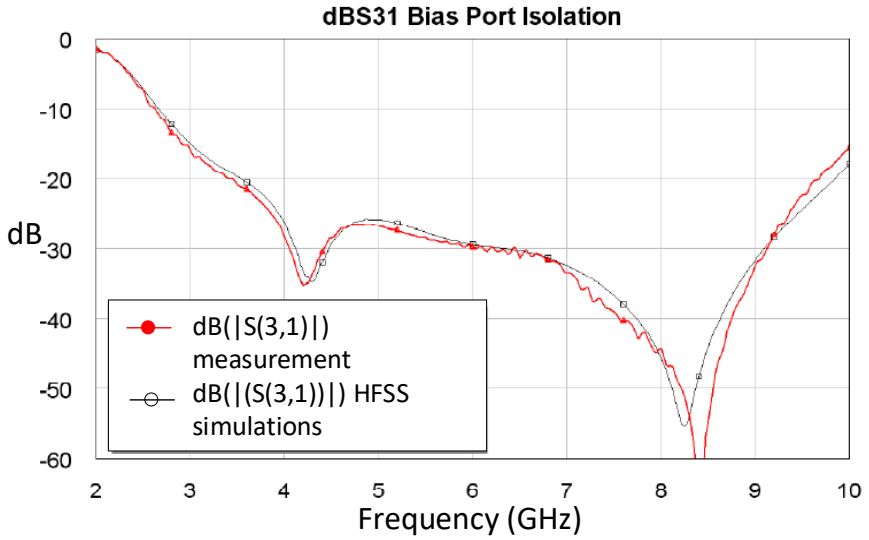

Figure 4.1.4: Signal transmission from port 1 to port 3. The black line represents the simulations, while the red line denotes the measurements (Kooi, 2005).

Jacob Kooi, from CALTECH, directly provided the circuit characteristics and transmission line dimensions for these simulations. Figure 4.1.5 illustrates the circuit model employed in constructing the TDR. This model served as the foundation for developing the complete HFSS circuit model, as depicted in the figures from the following sections.

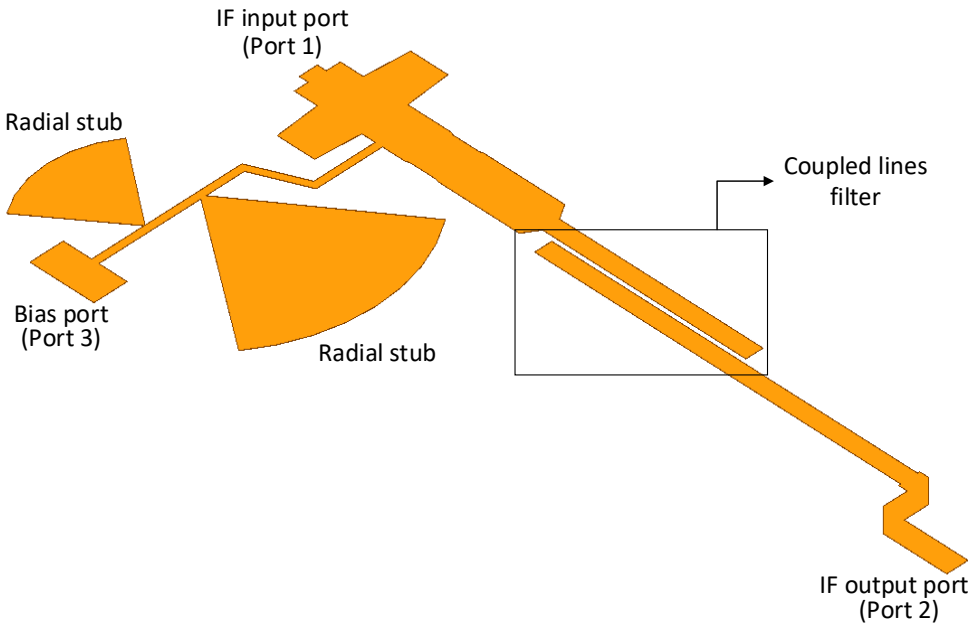

Figure 4.1.5: Microstrip IF circuit model in HFSS, each component has been labeled. The large stub was designed to block low frequencies, while the small stub was intended to suppress high frequencies, both within the operational bandwidth.

4.2 Replication of the TDR Model in HFSS.

In this section, the construction of the TDR model is presented. The description begins with an overview of the entire module, followed by a comprehensive analysis of its various components. The image 4.1.1 illustrates the original TDR tested by Jacob Kooi. The HFSS model has to simulate this module in order to proceed with the modifications. It is important to know that multiple HFSS models of the TDR were attempted; however, they did not yield the desired solutions.

Subsequently, various configurations were assessed within the model by altering specific parameters such as port size and shape. Adjustments were made to the dimensions of the vacuum column, connectors were introduced, and corrections were implemented in the geometry of the design. The primary objective behind these modifications was to emulate the performance characteristics of the original TDR.

4.2.1 TDR Model Construction

In order to achieve results that closely match the measurements and simulations conducted by Jacob Kooi, the initial step was to import the microstrip design of the circuit into HFSS. Figure 4.1.5 illustrates the IF circuit model, with each component clearly labeled, it was designed to operate within a 3-9 GHz bandwidth. The conductor material for the microstrip structure is gold.

The signal received by the IF input port comes from the SIS mixer, passes through the coupled lines filter, which effectively eliminates the DC current and harmonics, and then proceeds to the IF output port. The two radial stubs were designed to prevent undesired signals (with frequencies in the IF band) from coming from the Bias port to the IF port. They have different dimensions to stop different frequency bands; the big radial stub was designed to block frequencies between 3.5 to 5.5 GHz approximately, and the small stub was thought to stop IF signals from 7.5 to 9 GHz approximately.

The next step involved incorporating the substrate and the vacuum column, as indicated by Jacob Kooi in his doctoral thesis (Kooi, 2008). The material used for the substrate was alumina, and the dimensions are provided in the following table:

Substrate	ϵ_r	H_{sub} (μm)	W (μm)	L (mm)	S (μm)	H_{cav} (μm)	H_{air} (mm)	W_c x L_c (mm)
Alumina	9.90	635	480	5.72	120	585	2.5	5.08 x 6.1

Table 4.2.1: ϵ_r correspond to the relative permittivity of the substrate, H_{sub} is the substrate hight, W is the width of the coupled lines, L is their lenght, S is the gap of the coupled lines, H_{cav} is the cavity depth, H_{air} is the height above the substrate, L_c is the cavity length, and W_c is the cavity width Kooi (2008).

The parameters referred to the cavity height, length, and width correspond to the cavity below the alumina plate. It is part of the module and works as a resonator for the filter. Figure 4.2.1 illustrates the dimensions listed in the previous table.

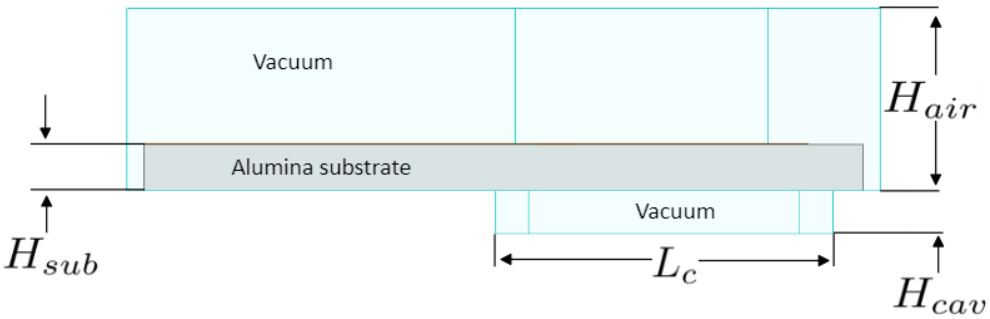

Figure 4.2.1: The dimensions of the module housing the alumina circuit board are depicted here. The segment shaded in light blue represents the vacuum region. The grey segment represents the substrate.

Figure 4.2.2 illustrates the dimensions of the coupled lines filter as mentioned in the previous table.

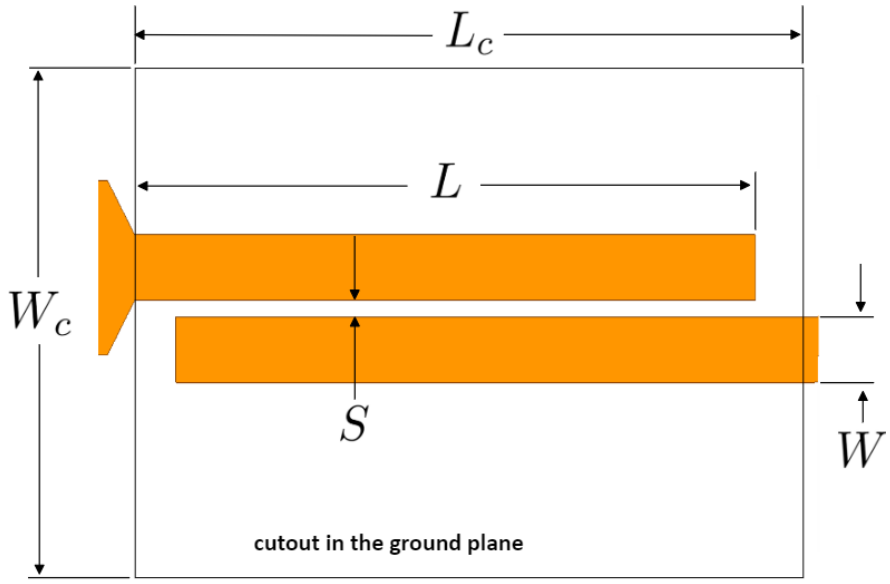

Figure 4.2.2: Coupled lines dimensions. The cutout in the ground plane has the dimensions of the cavity.

The following step was to incorporate the ground plane, which has a cutout just below the coupled lines filter. Figure 4.2.3 shows the ground plane installed on the substrate, through the cutout we can see the alumina. The thickness of the ground plane is 3.81 μm and is made of gold, the same as the transmission line. This ground plane is connected to the bottom metallic chassis of the module, which has a reduction of height H_{cav} in the filter cavity space (as depicted in Figure 4.2.2)

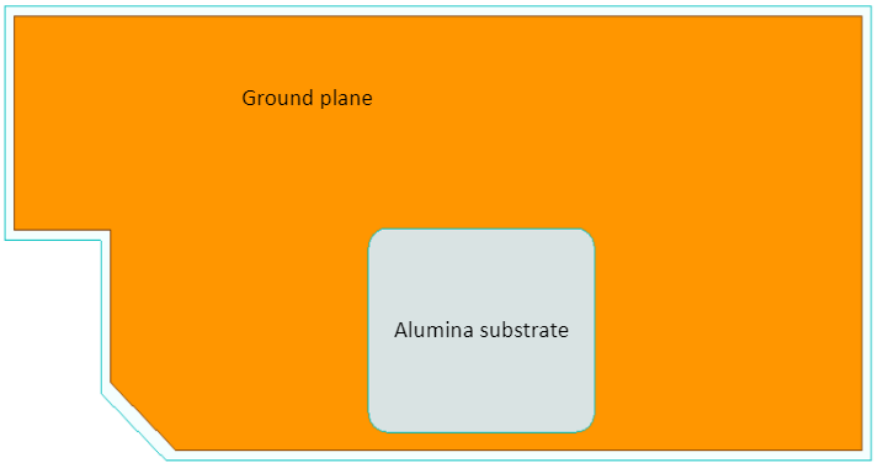

Figure 4.2.3: Ground plane installed on the substrate. The alumina is visible through the cutout

Then, the ports were integrated into the model. In order to make them similar to SMA connectors the ports have a circular shape. The input IF port has an impedance of 20 Ohm (port 1), whereas the Bias (port 3) and output IF ports (port 2) have 50 Ohm. The different impedance of port 1 is required for the correct operation of the SIS mixers. The ports were positioned at 254 μm from the circuit board, precisely at the border of the vacuum column, this spacing was the same as the existing in the original TDR.

Cylindrical connectors were introduced between the ports and the circuit to replicate the interconnection of genuine SMA connectors in contact with the conducting line. Moreover, the contact area of these cylindrical connectors was enlarged using rectangles to simulate soldering. Figure 4.2.4 shows the connector of the IF input port as an example.

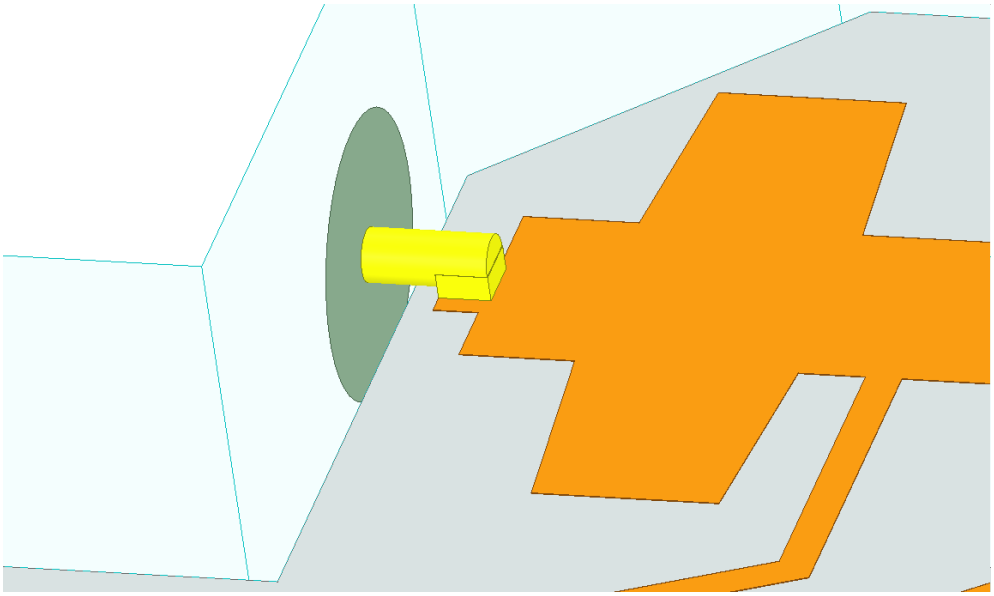

Figure 4.2.4: Connector and port in the circuit model. Here the IF input port, or port 1, is shown.

Finally, the definitive version of the HFSS TDR model is illustrated in figure 4.2.5. The results of the simulations are shown in the next section.

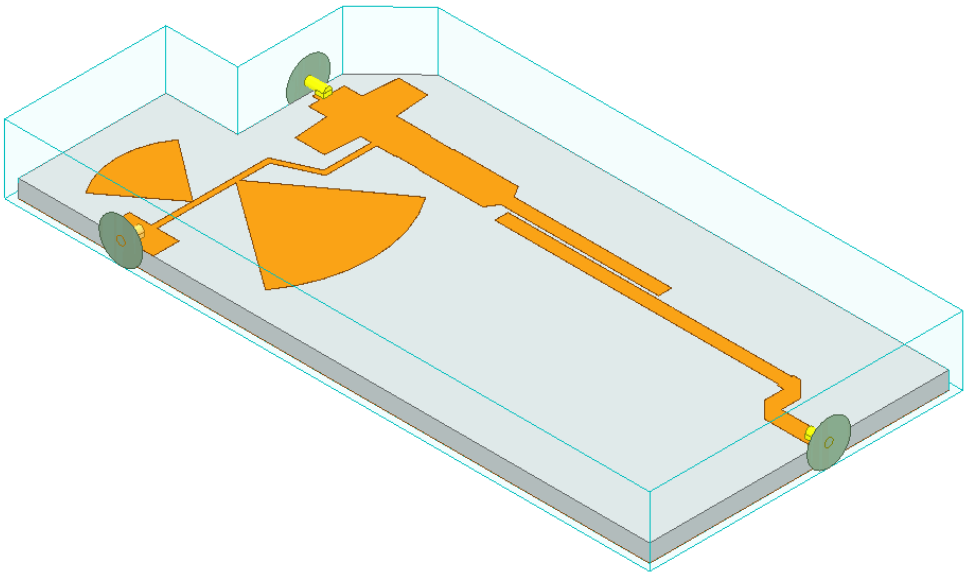

Figure 4.2.5: Replication of the HFSS TDR model, LCT version. This model will be used to start with the modifications on the transmission lines.

4.2.2 TDR Simulation.

Upon finalizing the TDR model construction, the simulation phase began. HFSS required approximately 10 minutes to execute these simulations and subsequently presented the outcomes through its dedicated graphs. Furthermore, the software offered the flexibility to extract simulation data in various formats. To enhance result visibility in this instance, the simulation data was extracted from HFSS in ".txt" format and subsequently utilized to generate graphs using Python.

The HFSS simulation results of the preceding model are depicted in Figures 4.2.6, 4.2.7, and 4.2.8. These figures juxtapose the current simulations with the simulations and measurements of Jacob Kooi's TDR (Kooi, 2005). Here, it is shown the reflection parameter in port 1 (S11), the transmission parameter from port 1 to port 2 (S21), and the transmission parameter from port 1 to port 3 (S31). A comparison with the original measurements and simulations conducted by Jacob Kooi is illustrated in the Discussion section.

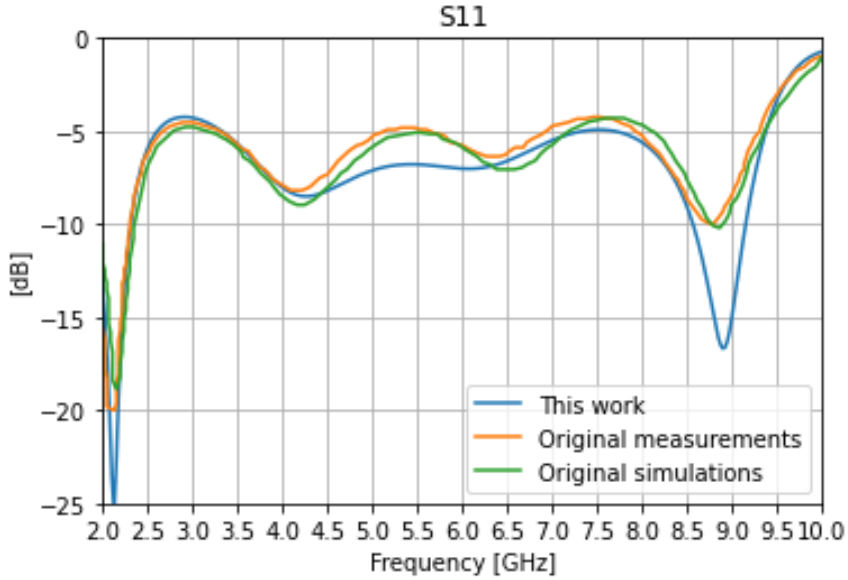

Figure 4.2.6: Comparison of the S11 parameter. The blue line corresponds to the simulations conducted in this work, the orange line represents measurements of the TDR carried out by Jacob Kooi, and the green line signifies simulations also performed by Jacob Kooi for the TDR.

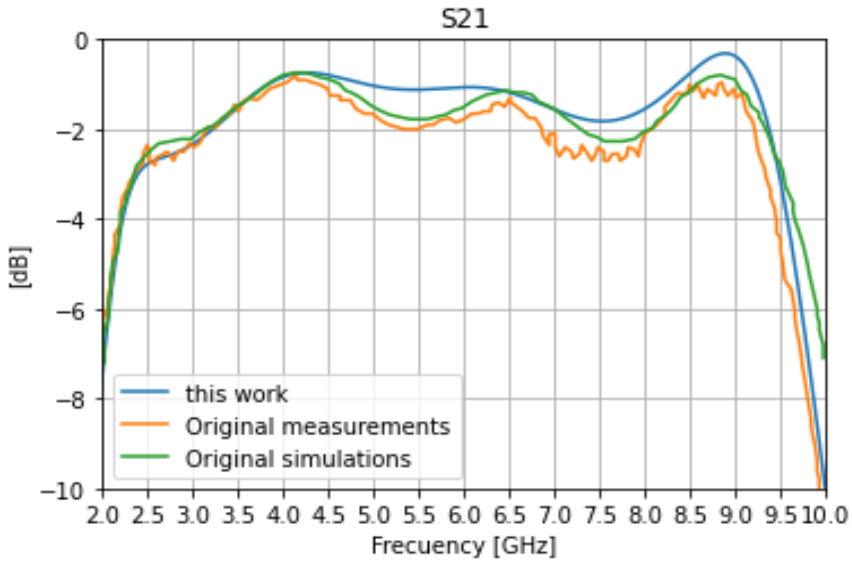

Figure 4.2.7: Comparison of the S21 parameter. The blue line corresponds to the simulations conducted in this work, the orange line represents measurements of the TDR carried out by Jacob Kooi, and the green line signifies simulations also performed by Jacob Kooi for the TDR.

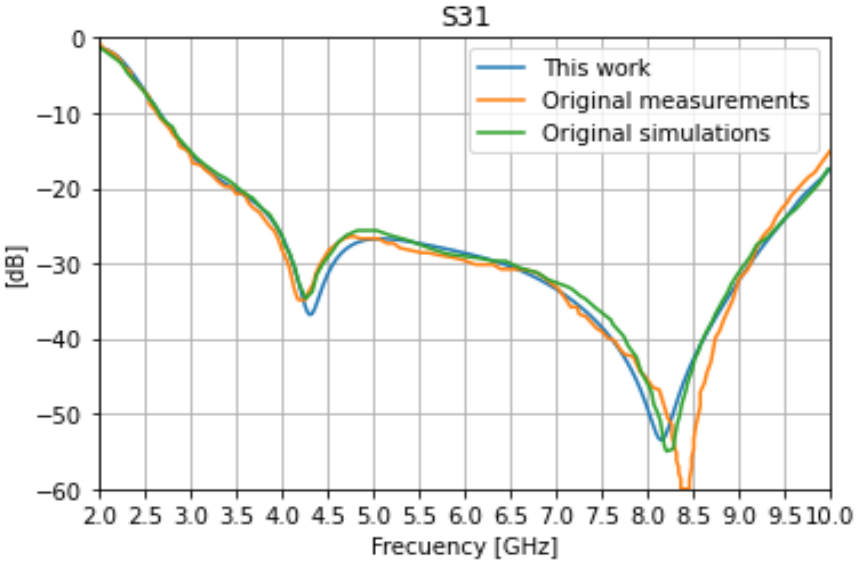

Figure 4.2.8: Comparison of the S31 parameter. The blue line corresponds to the simulations conducted in this work, the orange line represents measurements of the TDR carried out by Jacob Kooi, and the green line signifies simulations also performed by Jacob Kooi for the TDR.

While the outcomes may not align precisely with the original simulations or measurements, they provide almost the same response and show most of

the operational characteristics of the IF circuit. Consequently, the successful replication of the TDR's performance was deemed accomplished. The following steps are the modification of the circuit aimed at broadening the bandwidth of the IF signal, investigating the implementation of sideband separation, and integrating these adjustments into the final design.

4.3 Modifications to the IF Circuit Board.

4.3.1 Modifications to the original transmission line.

Upon the TDR model providing good enough simulation results, the circuit modification started. A distinct model was created in a separate file to serve as the basis for the entire circuit, incorporating the necessary alterations.

Independently, AWR's Ifilter Wizard was employed in an attempt to devise novel filters that fulfill the requirements. Variants involving shunt stubs and coupled lines filters were explored; however, these configurations proved unsuccessful due to issues with impedance conditions and the establishment of transmission zero (TZ) for the DC signal. The TZ requirements establish that DC voltages introduced in the Bias port should not be observed at the output port, to ensure that the bias signals configured on the mixers at this port are not modified.

The first part of the IF circuit to be modified was the radial stubs. To increase the bandwidth of the IF signal response, a 0.5 mm cutting was made to the stubs to disconnect them from the bias line as shown in figure 4.3.1.

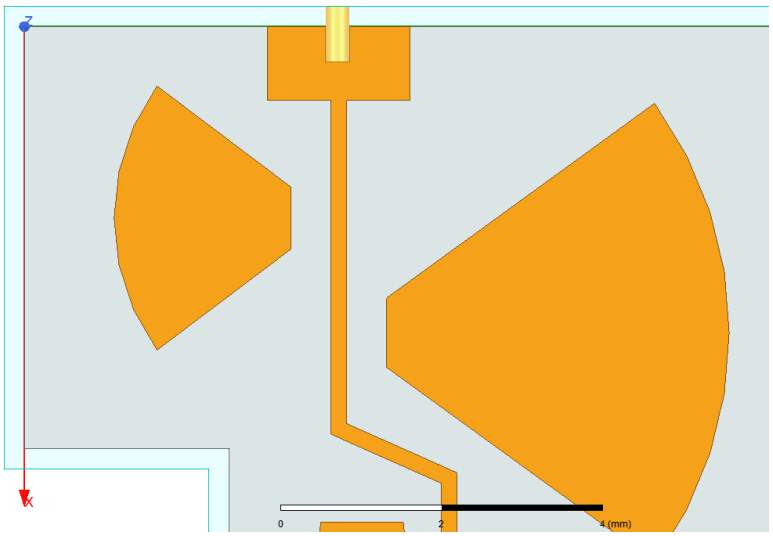

Figure 4.3.1: HFSS model of the circuit with modifications. Disconnection of the stubs.

Subsequently, the coupled lines filter was bypassed by incorporating 18 gold bond wires to interconnect each line, effectively converting it into a transmission line. This transformation is illustrated in Figure 4.3.2.

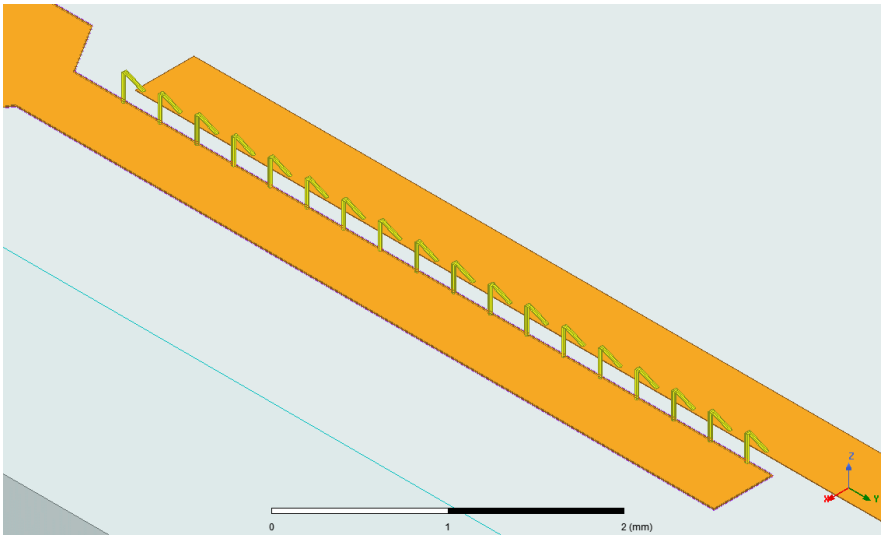

Figure 4.3.2: Bypassing of the coupled lines filter by the use of bond wires connecting each line of the filter.

The next alteration to the circuit involved the exclusion of the Wilkinson summing node. Presently, both branches of the circuit exit autonomously, enabling the acquisition of each signal separately. Figure 4.3.3 illustrates the new lines replacing the Wilkinson summing node.

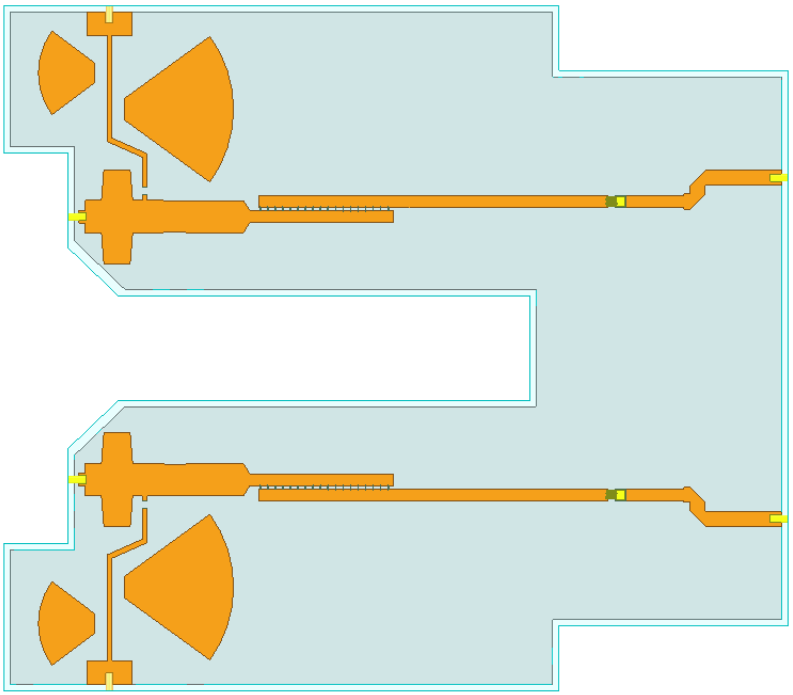

Figure 4.3.3: Complete circuit without the Wilkinson summing node, the stubs disconnection is also visible.

4.3.2 Integration of passive components.

The removal of the aforementioned components requires the addition of new components that provide a similar response, but generate an increased IF bandwidth. To broaden the bandwidth of the IF signal, the introduction of passive components was the selected course of action. Nevertheless, the chosen components must meet specific criteria, including reliable stability in cryogenic conditions and mechanical durability when subjected to temperature variations.

The subsequent components have been chosen due to their adherence to the previously stated prerequisites. They underwent testing at cryogenic temperatures as low as 4K and exhibited minimal performance fluctuations (Lamb, 2014). The fabrication processes and material properties render them suitable for use in simulations and eventual integration into the circuit.

• **The 300 Ohm Resistor:** Removing the radial stubs reduces the attenuation of the IF signal transmission between port 1 and port 3. To achieve a similar outcome as the stubs while expanding the IF signal bandwidth, a 330 Ohm resistor was positioned at the juncture of the main line and the bias line. Figure 4.3.4

illustrates the bias line cut and the inclusion of the resistor.

The selected component was the VISHAY CH0402FP330R, where the "CH" denotes the global model, "0402" represents the chip size, "F" signifies flip chip (SnAg over nickel barrier), "P" stands for one face (gold bonding pads), and "330R" indicates the Ohmic value.

To make the HFSS model as real as possible, the S parameters of the resistor were obtained from the stockist's website (Mouser Electronics, 2023). The S2P file (Touchstone format) downloaded has information on the S parameters from 0.1 to 49.6 GHz. Subsequently, the parameters were imported into HFSS and assigned to lumped ports, facilitating simulations employing the intended resistor model.

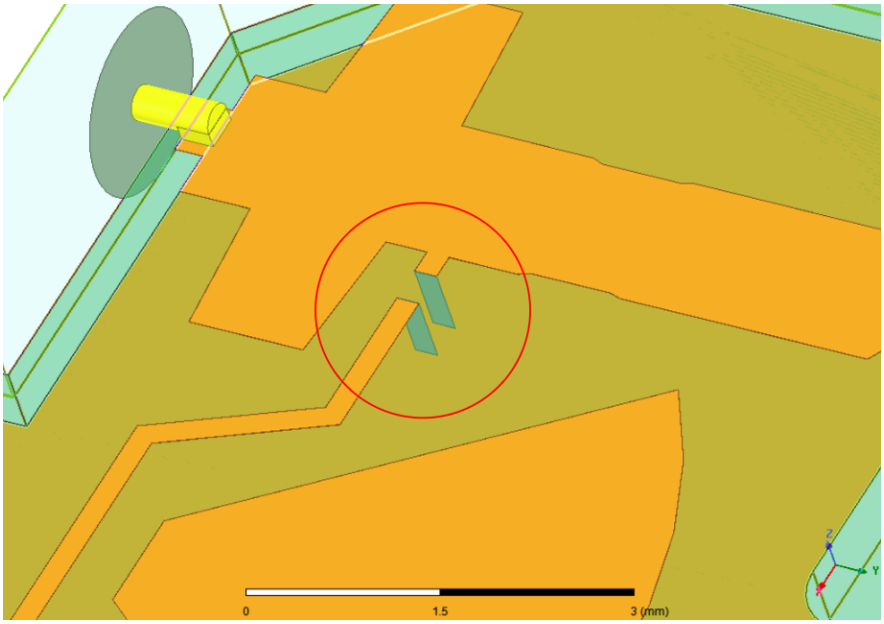

Figure 4.3.4: HFSS model of the circuit: the red circle indicates the cut in the bias line and the placement of the resistor. The substrate was rendered transparent to enhance the visualization of the lumped ports (identified as grey rectangles) connecting the conducting lines to the ground.

• **The 68 pF Capacitor:** With the removal of the Wilkinson summing node, two distinct transmission lines carry the IF signal from each mixer out of the module. Conversely, the absence of the coupled lines filter permits the DC signal and harmonics to reach the IF output port. To address this issue, a cut was made in the transmission line adjacent to the former coupled lines filter, and within this cut, a capacitor was inserted. Figure 4.3.5 illustrates the cut in the transmission lines and the inclusion of the capacitor.

The chosen capacitor for the simulation was the Skyworks SC06801518, where the "SC" stands for the global model, "68" represents the capacitance in pF, and "1518" indicates the pad dimensions in mils.

Similarly, as in the case of the resistor, the S parameters were sourced from the manufacturer's website (Skyworks Solutions, 2023). The downloaded S2P file (Touchstone format) has information on the S parameters from 0 to 10 GHz. These parameters were imported to HFSS and linked to lumped ports, streamlining simulations that utilize the designated capacitor model.

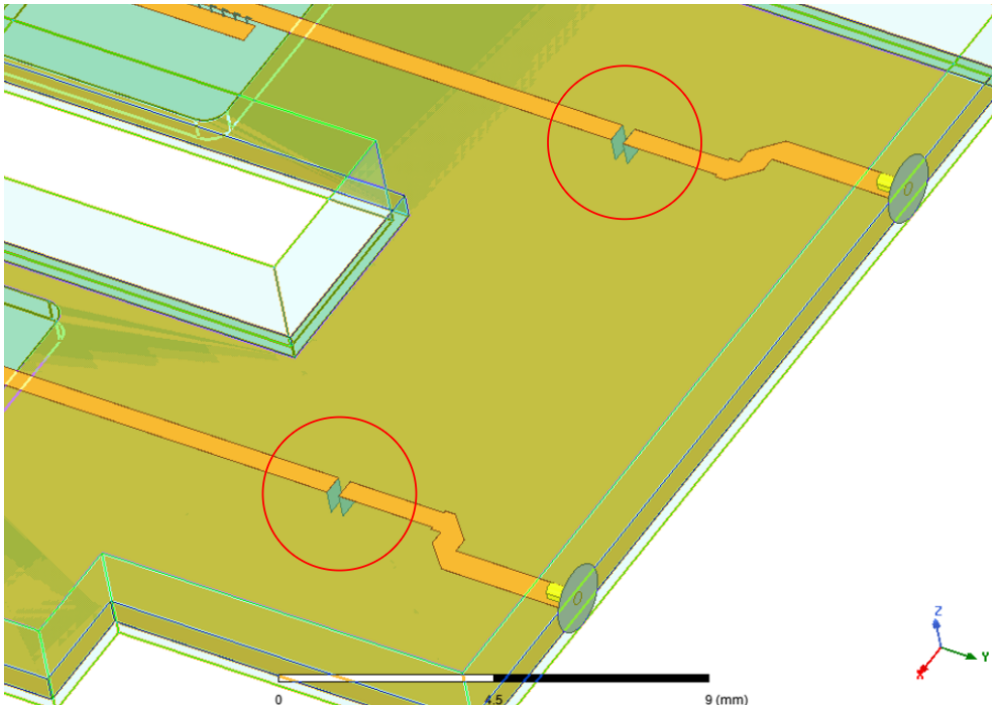

Figure 4.3.5: HFSS model of the circuit: The red circles indicate the cut in the transmission lines and the placement of the capacitor. The substrate was rendered transparent for better visualization of the lumped ports (identified as gray rectangles) connecting the transmission lines to the ground.

Figure 4.3.6 illustrates the proposed installation of the capacitor in the new IF circuit design of the LCT receiver. Bond wires will be employed to connect the two sections of the transmission lines. The IF signal will pass through the capacitor for filtering and then be directed to the IF output port (port 2).

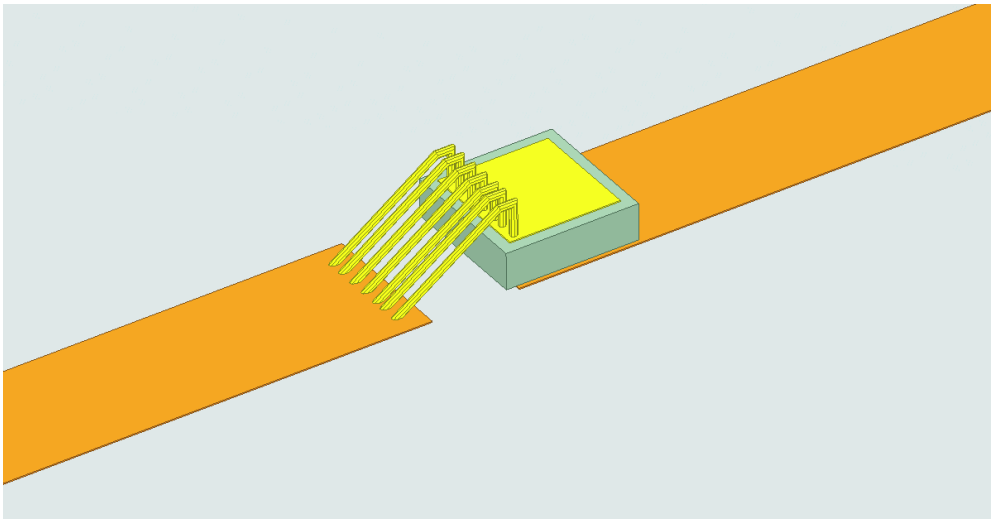

Figure 4.3.6: HFSS model of the circuit. One conducting layer of the capacitor (yellow square) will be soldered to the section of the transmission line (orange rectangles) directed towards the output. Meanwhile, the other layer will be in contact with the first section of the transmission line through bond wires.

The completely new design of the circuit is shown in figure 4.3.7. Here we can observe that each branch has its output. It is important to note that this modification necessitates altering the mechanical part of the packaging module to accommodate a new IF output port. This is the new IF circuit design of the LCT receiver.

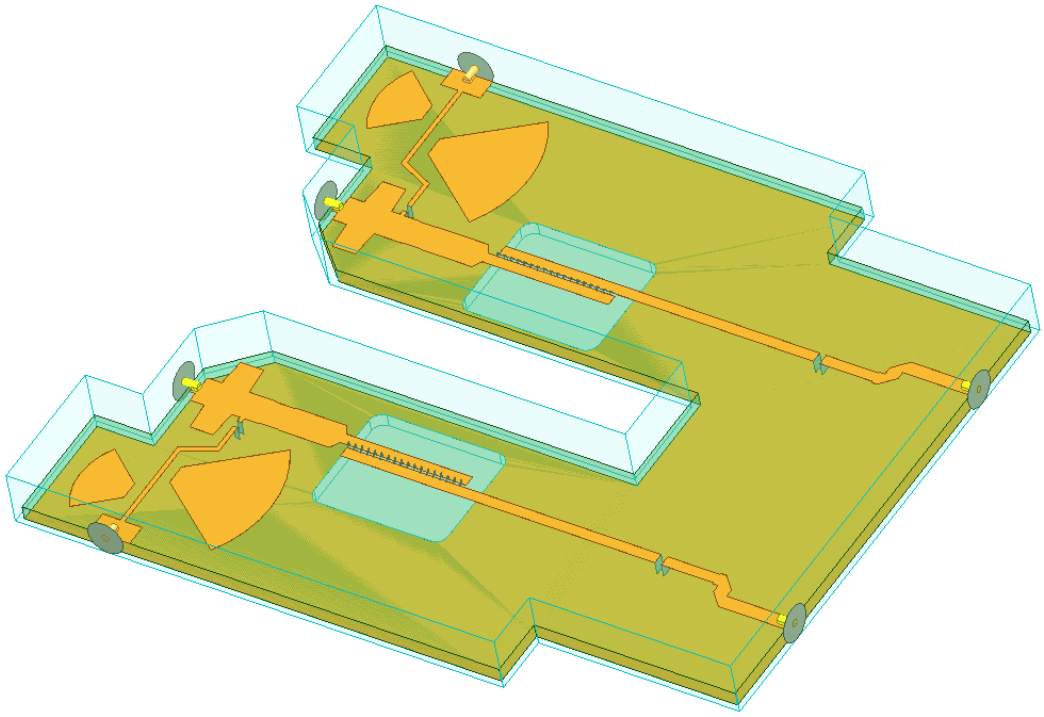

Figure 4.3.7: HFSS model of the new circuit design. The substrate was rendered transparent to enhance visualization of the lumped ports and the ground cut.

4.3.3 New Design Results.

Upon finalizing the HFSS model for the novel circuit design, a simulation was executed. The S parameter data obtained from the passive component enabled the acquisition of simulation data up to 10 GHz. For obtaining the simulation outcomes, S parameters were extracted from the HFSS model presented in figure 4.3.7. To achieve this, a ".txt" file was extracted from HFSS and imported into Python to generate a plot.

The outcomes of the updated design are depicted in figure 4.3.8. The S31 parameter remains exceptionally low, implying that the resistor in the bias line effectively accomplishes its intended function. The S11 parameter remains consistent with the original measurements conducted by J. Kooi, signifying that the newly introduced components within the circuit do not influence the reflection of the IF signal. Consequently, the IF circuit board's enhanced bandwidth, represented by the S21 parameter, now spans from 0.06 to 9.3 GHz, presenting a wider spectrum than the previous 4 - 8 GHz bandwidth.

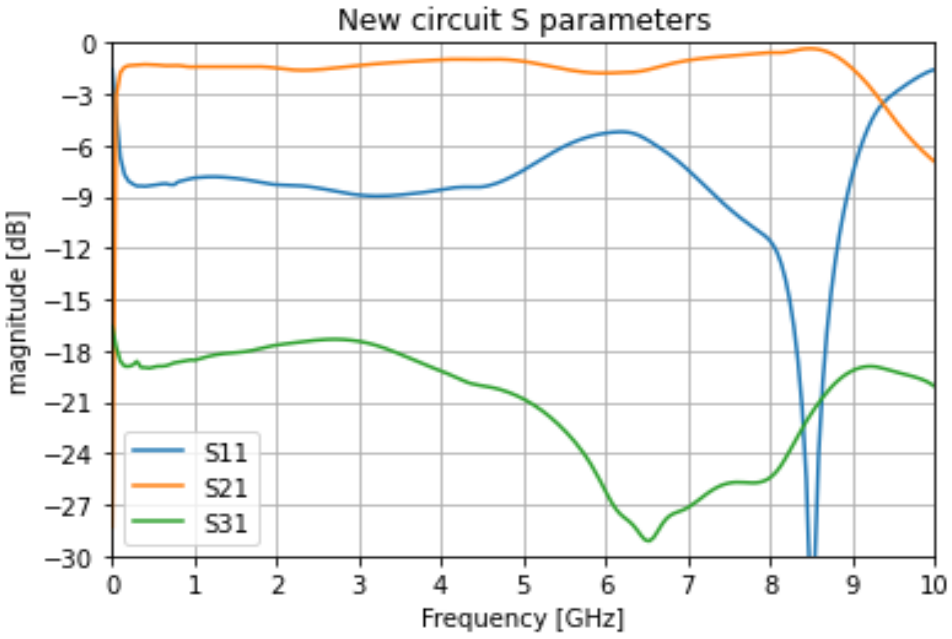

Figure 4.3.8: Simulation results for the new design of the IF circuit board. The reflection of the IF signal (S11 parameter) is represented by the blue line. The transmission of the IF signal (S21 parameter), is represented by the orange line. The transmission of the IF signal from port 1 to port 3 (S31 parameter) is represented by the green line.

4.3.4 Comparison Between Original TDR and the New Design

The results obtained in the simulations have shown that the bandwidth of the receiver can be enhanced. However, this section provides a comparison between the outcomes of the new design and the simulations conducted by Jacob Kooi in the Technology Demonstration Receiver.

Figures 4.3.9, 4.3.10, and 4.3.11, show the previously mentioned comparison. An important observation needs to be made. J. Kooi conducted the measurements and simulations of the TDR in the 2 to 10 GHz range, which is the reason for the lack of information in the 0 to 2 GHz range. In this thesis, the simulations of the new design cover the 0 to 10 GHz range.

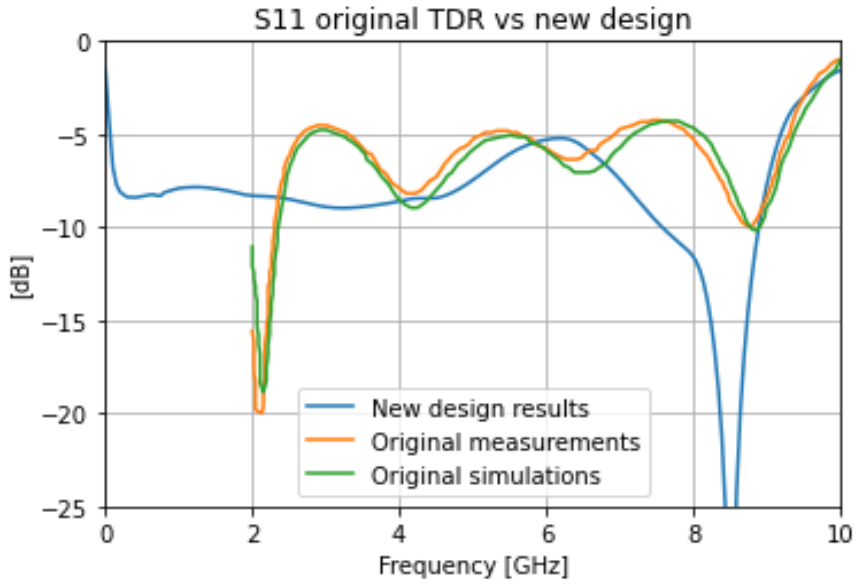

Figure 4.3.9: S11 parameter, comparison between the new design results obtained in the HFSS simulations and Jacob Kooi's simulations of the TDR.

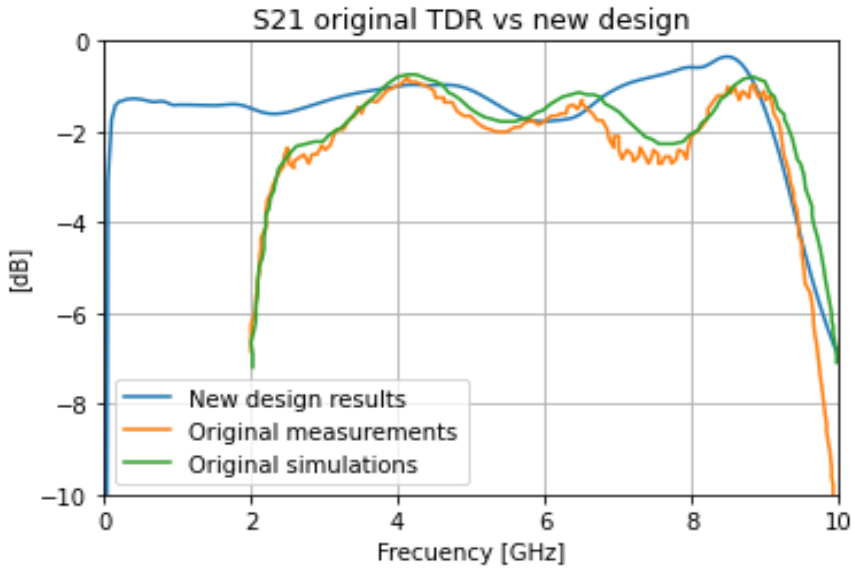

Figure 4.3.10: S21 parameter, comparison between the new design results obtained in the HFSS simulations and Jacob Kooi's simulations of the TDR.

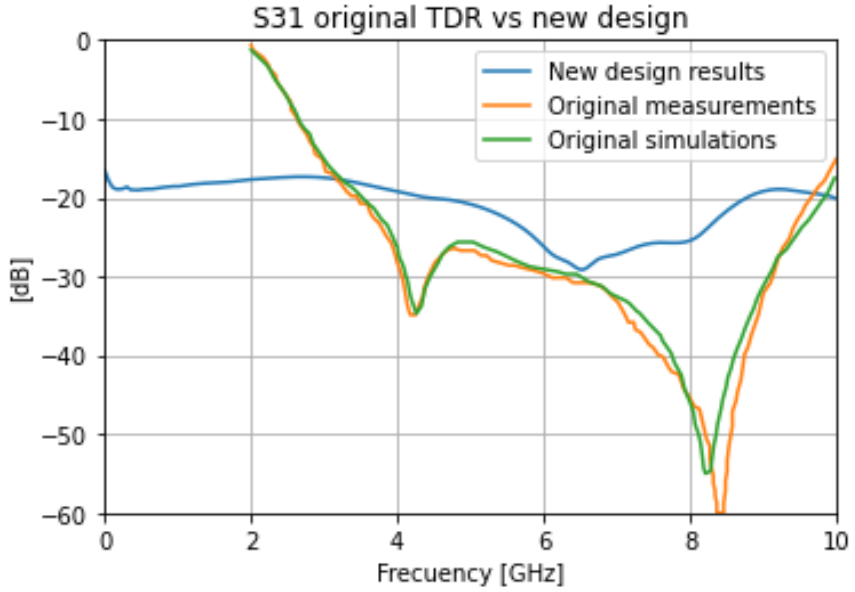

Figure 4.3.11: S31 parameter, comparison between the new design results obtained in the HFSS simulations and Jacob Kooi's simulations of the TDR.

To better understand the receiver improvement, Figure 4.3.12 illustrates the bandwidth of Kooi's simulation of the TDR and the new design simulation. It

shows that the lower frequencies have a more significant improvement, while the higher frequencies have a slight reduction.

To determine the bandwidth, the maximum value of both curves was marked with a solid horizontal line, red for this work and black for Kooi's simulations. From this value, a drop of 3 dB was also marked with dotted horizontal lines, red for this work and black for Kooi's simulations. The points where these lines intersect with the curves were marked with dotted vertical lines, magenta for this work and green for Kooi's simulation. This way, we can identify the bandwidth of both curves.

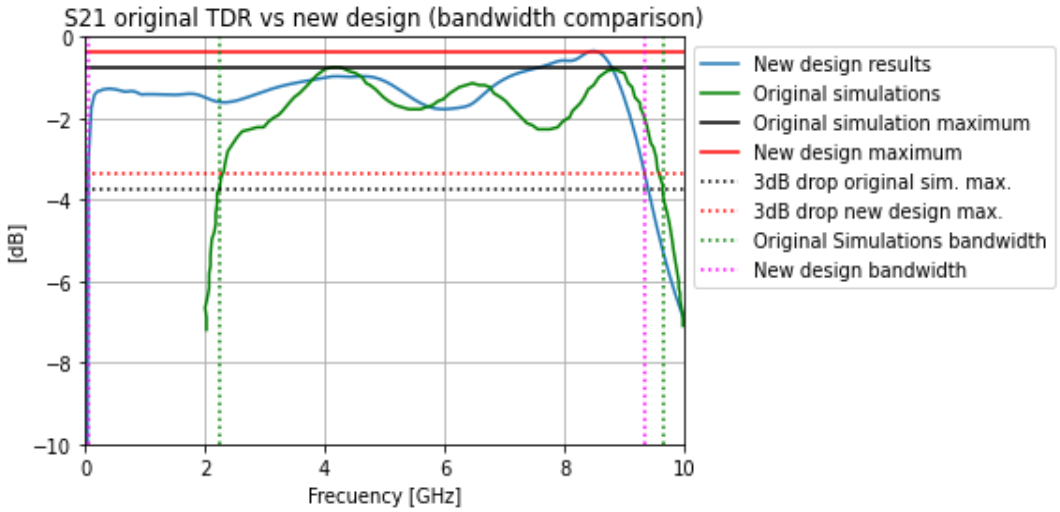

Figure 4.3.12: Comparison between the bandwidth achieved in the new design and the original TDR using the S21 parameter. The bandwidth of the original simulation is marked with the green dotted vertical lines, while the bandwidth of the new design is marked with the magenta dotted vertical lines.

In figure 4.3.12 we can identify the bandwidth of both curves. For Kooi's simulation of the TDR, the bandwidth is 7.4 GHz, and for the new design of the IF circuit, it is 9.3 GHz.

It is important to mention that this is a comparison with the Technology Demonstration Receiver, which is not the complete original circuit used in the CSO. As mentioned in Kooi (2008), the original circuit has a bandwidth that spans from 3 to 9 GHz, i.e., a 6 GHz bandwidth. Moreover, it is mentioned that due to limitations imposed by the LNA at the IF output, the final bandwidth is 4 GHz, a problem that is expected to be solved due to access to new LNA technology.

Given the results obtained, the next step was to calculate the ripple. To complete this task, Python code was used in order to work with the files containing the S parameters from the simulations of this thesis and J. Kooi's HFSS simulations of the TDR.

The procedure was to calculate the mean of dB values; and determine the maximum value in between the bandwidth of each simulation. Then, the ripple is the subtraction of these values.

Finally, the ripple for J. Kooi's simulation is 1.0463 dB. For this thesis's new design simulation, the calculated ripple was 0.9168 dB.

4.4 AWR Simulations: Lumped elements analysis

The AWR software proved to be an efficient tool for conducting rapid simulations with various passive components added to the new circuit design. It offers the flexibility to modify the components' characteristics and swiftly execute simulations, yielding graphs with the S parameters of the circuit.

However, AWR was not deemed the primary simulation software because it does not support three-dimensional simulations as HFSS does. Consequently, the results obtained with AWR are not as precise as those from HFSS.

On the other hand, to validate the correctness of the resistance values of the passive components, simulations were conducted in AWR. S parameters from the simulations of the modified TDR (with the 68 pF capacitor as bandpass filter) conducted in HFSS were extracted and imported into AWR. Then, a resistor was introduced to the circuit, and simulations were performed to ensure that the choice of the resistor for the final simulations and its subsequent implementation were accurate and did not adversely impact the overall circuit's performance.

The primary reason for conducting AWR simulations of the circuit was the absence of S parameters for the chosen resistor (300 Ohm) intended for use in the new circuit design. The rationale behind using the 300 Ohm resistor was related to the component's size, which was compatible with the transmission line. The S parameters utilized in the simulations presented in the Results section correspond to a 330 Ohm resistor. Figure 4.4.1 depicts the integration of the HFSS S parameters of the TDR into AWR, where a 330 Ohm resistor is connected to the

TDR. In this scenario, the bandwidth spans from 0.093 to 9.536 GHz as illustrated in figure 4.4.2.

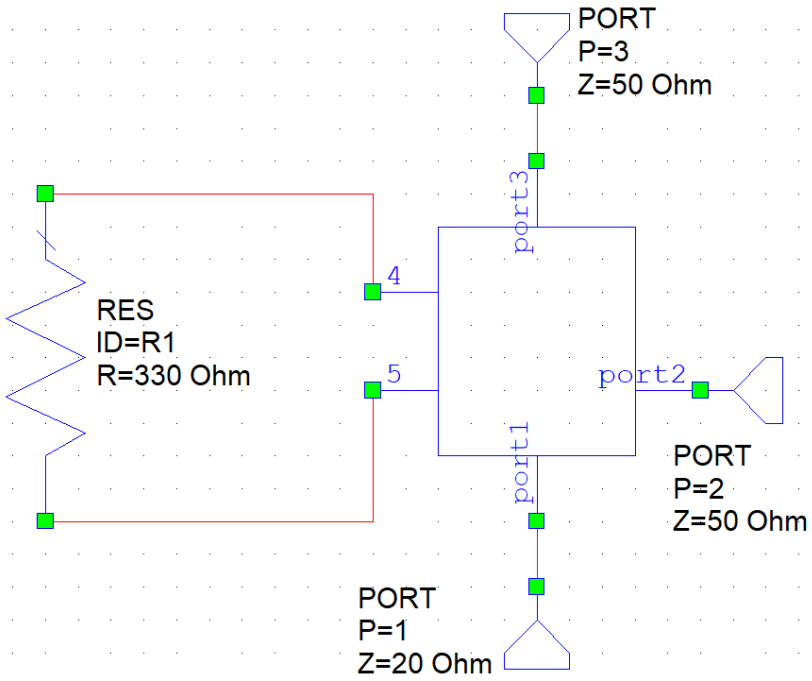

Figure 4.4.1: In the TDR model created in AWR, a 330 Ohm resistor was connected to the block where the S parameters from HFSS were uploaded. Ports 1, 2, and 3 represent the IF signal input, IF signal output, and the bias port, respectively. Ports 4 and 5 were added to facilitate the connection of the resistor to the block and represent a discontinuity in the bias line.

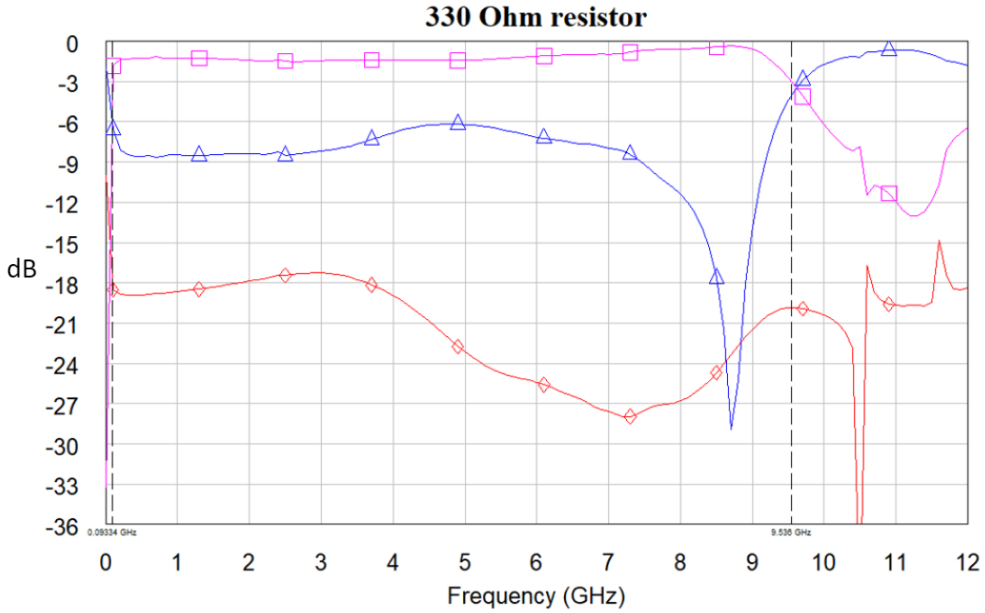

Figure 4.4.2: The results of implementing a 330 Ohm resistor are displayed. The pink line represents the S21 parameter, the blue line signifies the S11 parameter, and the red line represents the S31 parameter.

The difference in bandwidth compared to that obtained in the HFSS simulations is attributed to the inability to perform 3D simulations in AWR.

Another simulation was conducted using a 300 Ohm resistor to facilitate a comparison with the previous resistor. Figure 4.4.3 illustrates the sole modification made to the AWR model. In figure 4.4.4, we observe the simulation results, which depict a bandwidth ranging from 0.104 to 9.536, resulting in a 0.011 GHz difference between the bandwidths of both models.

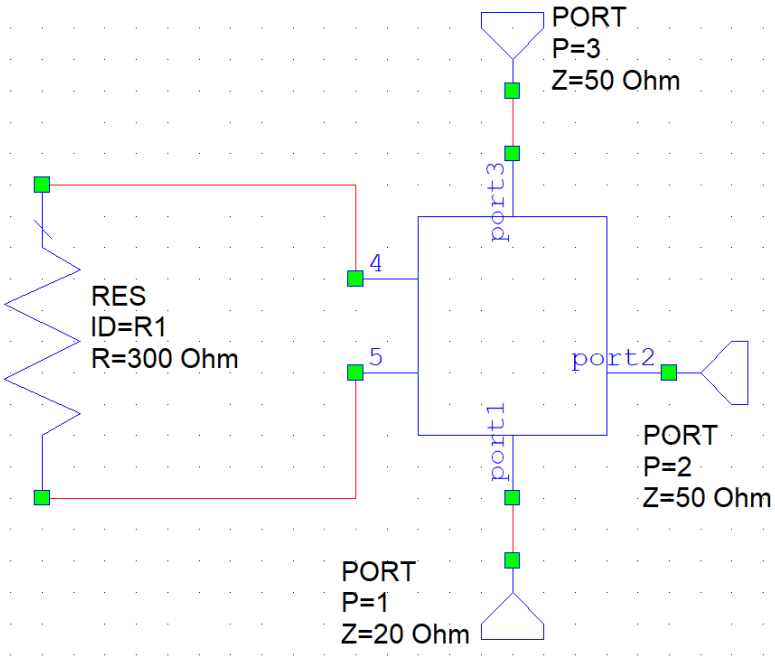

Figure 4.4.3: In the TDR model created in AWR, a 300 Ohm resistor was connected to the block where the S parameters from HFSS were uploaded. As in the previous model, ports 1, 2, and 3 represent the IF signal input, IF signal output, and the bias port, respectively. Ports 4 and 5 were added to facilitate the connection of the resistor to the block and represent a discontinuity in the bias line.

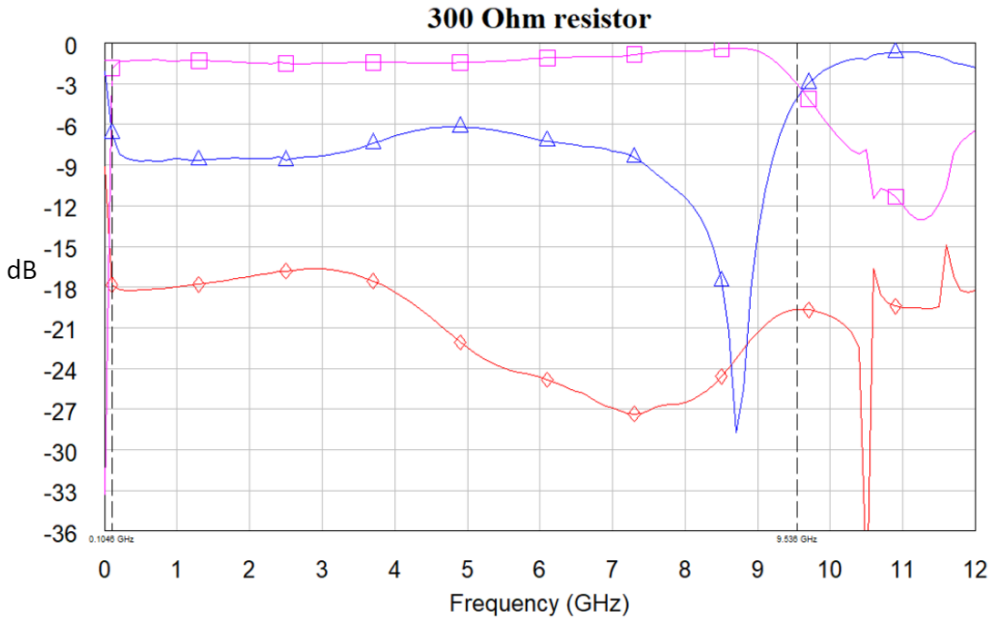

Figure 4.4.4: The results of implementing a 300 Ohm resistor are displayed. The pink line represents the S21 parameter, the blue line signifies the S11 parameter, and the red line represents the S31 parameter.

Simulations in AWR were carried out using the data from the HFSS simulation of the new TDR, which included a 68 pF capacitor serving as a bandpass filter. In these simulations, two resistors were added to the circuit for comparison, aiming to demonstrate that there is no significant difference in the bandwidth generated by these components.

From this experiment, the results revealed a difference of 0.011 GHz between the bandwidths, which can be considered insignificant. Therefore, it can be concluded that the use of S parameters of the 330 Ohm resistor in the definitive HFSS simulation of this thesis does not pose an issue when implementing the new design of the IF circuit, which will employ a 300 Ohm resistor.

4.5 Application of the 2SB Scheme in the Circuit.

One of the aims of this thesis was to evaluate the feasibility of the implementation of a sideband separating (2SB) architecture within the IF circuit. The concept involves isolating the signals from each branch within the module independently and subsequently routing them through a digital hybrid. This hybrid operation would lead to the independent extraction of the upper sideband (USB) and the lower sideband (LSB) from each output of the hybrid.

In this context, the feasibility of incorporating a 2SB architecture into the IF circuit was investigated. The core concept involved integrating a digital 90° or 180° hybrid at the output of the IF module. Subsequently, various calculations showcasing distinct configurations are presented to establish the practicality of this proposed implementation.

This segment provides a mathematical analysis of various configurations. The initial configuration involves a modification in which a 90° and a 180° hybrid are introduced at the IF circuit's output. Figure 4.5.1 visualizes the existing circuit with this initial modification. It is important to highlight that all the added components at the circuit's end are digital devices.

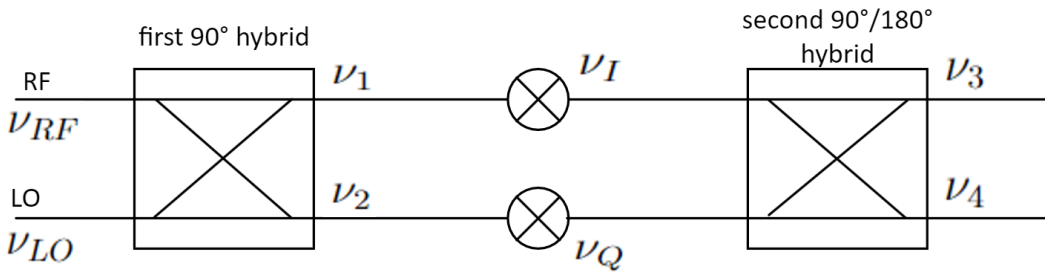

Figure 4.5.1: The present circuit configuration includes the incorporation of a second hybrid at the IF output.

In this experiment, the 90° hybrid was initially examined. The challenge arose when, upon implementing the phase adjustment introduced by the second hybrid, the anticipated cancellation of specific elements failed to materialize. As a result, the outcome was a combination of both the lower and upper sidebands, as demonstrated in the subsequent equations.

$$\nu_3 = V^U e^{-i(w_{IF}^U t+\frac{\pi}{2})} + V^L e^{-i(w_{IF}^L t+\frac{\pi}{2})} + V^U e^{-i(w_{IF}^U t-\pi)}) + V^L e^{-i(w_{IF}^L t-\pi)})$$

$$\nu_4 = V^U e^{-i(w_{IF}^U t)} + V^L e^{-i(w_{IF}^L t)} + V^U e^{-i(w_{IF}^U t-\frac{\pi}{2})} + V^L e^{-i(w_{IF}^L t-\frac{\pi}{2})}$$

Subsequently, the 180° hybrid was tested. Similar to the previous scenario, term cancellation is absent, as evidenced by the equations below.

$$\nu_3 = V^U e^{-i(w_{IF}^U t+\frac{\pi}{2})} + V^L e^{-i(w_{IF}^L t+\frac{\pi}{2})} + V^U e^{-i(w_{IF}^U t+\frac{\pi}{2})} + V^L e^{-i(w_{IF}^L t+\frac{\pi}{2})}$$

$$\nu_4 = V^U e^{-i(w_{IF}^U t - \frac{\pi}{2})} + V^L e^{-i(w_{IF}^L t - \frac{\pi}{2})} + V^U e^{-i(w_{IF}^U t - \frac{\pi}{2})} + V^L e^{-i(w_{IF}^L t - \frac{\pi}{2})}$$

In both study cases, the signals ν_3 and ν_4 are identical but with an additional phase displacement.

Another configuration was tested next. This time, both the RF and the LO signals are introduced into the first hybrid through a shared port, Figure 4.5.2 provides a visual representation of this arrangement. The second hybrid employed in this configuration is a digital 90° hybrid.

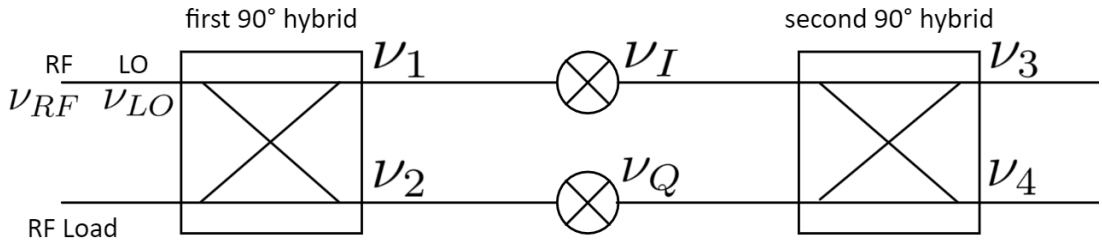

Figure 4.5.2: Configuration where both the RF and LO signals enter the first hybrid through the same port.

In this instance, term cancellation is absent, as demonstrated in the following equations. Once again we have not achieved the separation of the sidebands.

$$\nu_3 = V^U e^{-i(w_{IF}^U t)} + V^L e^{-i(w_{IF}^L t)} + V^U e^{-i(w_{IF}^U t - \frac{\pi}{2})} + V^L e^{-i(w_{IF}^L t - \frac{\pi}{2})}$$

$$\nu_4 = V^U e^{-i(w_{IF}^U t - \frac{\pi}{2})} + V^L e^{-i(w_{IF}^L t - \frac{\pi}{2})} + V^U e^{-i(w_{IF}^U t)} + V^L e^{-i(w_{IF}^L t)}$$

Now, moving on to the next configuration, it involves two 180° hybrids and a 90° phase shifter positioned before the hybrid denoted as H2. Specifics regarding this configuration are presented in Figure 4.5.3.

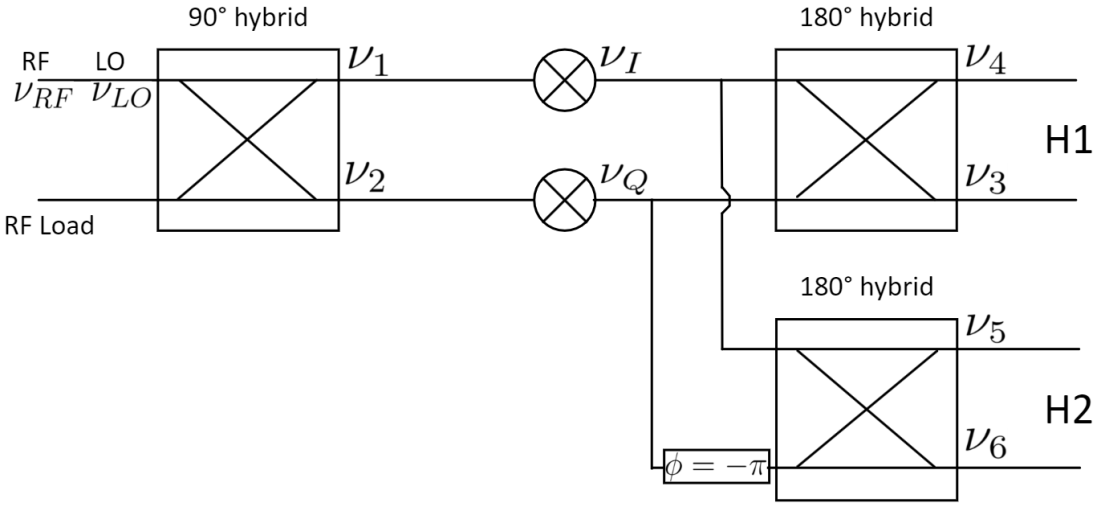

Figure 4.5.3: Arangement featuring two 180° hybrids, designated as H1 and H2. The latter includes a 90° phase shifter in one of its inputs.

Calculations were conducted individually for each hybrid. The following equations showcase the outcomes for H1.

$$\nu_3 = 2V^U e^{-i(w_{IF}^U t)} + 2V^L e^{i(w_{IF}^L t)}$$

$$\nu_4 = -2V^U e^{-i(w_{IF}^U t)} - 2V^L e^{-i(w_{IF}^L t)}$$

The following were the outcomes for H2.

$$\nu_5 = 2V^U e^{-i(w_{IF}^U t)} + 2V^L e^{i(w_{IF}^L t)}$$

$$\nu_6 = 0$$

The attempted setup involving two 180° digital hybrids yielded unsuccessful results. In both components, we encountered a summation of the sidebands. Furthermore, at the output port ν_6, sideband cancellation was observed. Finally, this configuration is incapable of achieving sideband separation.

In summary, this section has analytically demonstrated that achieving sideband separation is unattainable within this circuit. This limitation arises from the manner in which the RF and LO signals are introduced into the module and subsequently to the circuit board. When these signals share the same input, they consistently remain in phase, thereby preventing the separation of sidebands in

the digital hybrid system.

4.6 Proposal for the Sideband Separating System

As demonstrated in section 2.3.2, it is imperative for the LO signal to enter the mixer independently, separate from the RF signal. However, in the current module, both the RF and the LO signals are introduced to the mixer together.

Since the suggested alternative configurations proved ineffective due to the module design constraints, a distinct module arrangement is put forth to realize sideband separation within a digital hybrid system. Figure 4.6.1 illustrates the new configuration proposed for effectively generating sideband separation. The novelty lies in the revised input of the IF signal, which enters the SIS mixers independently, bypassing the initial 90° hybrid. Subsequently, the IF signal from each mixer is amplified before being routed to the IF processing module. Finally, it reaches the digital backend where the sideband separation takes place.

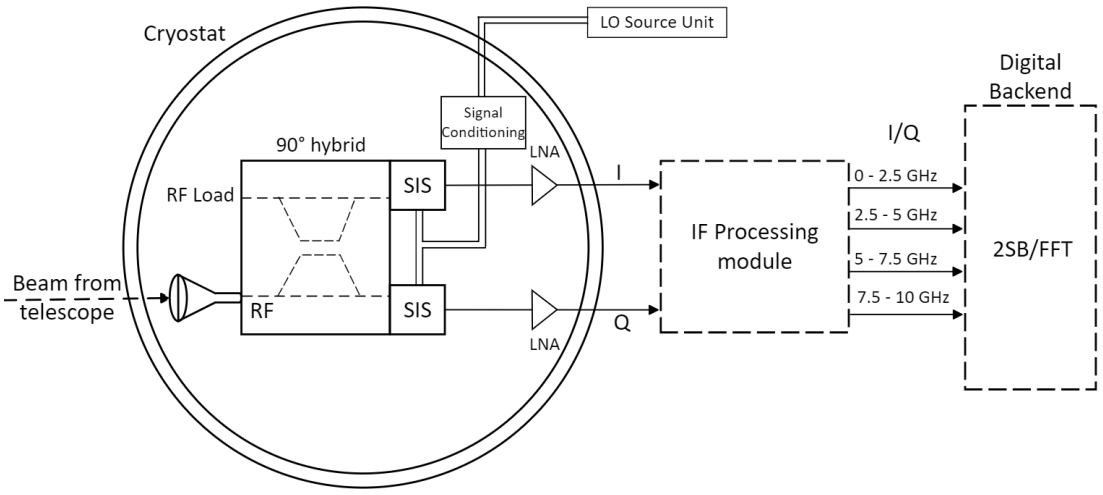

Figure 4.6.1: In the new receiver design proposal, the LO signal now bypasses the initial 90° hybrid and enters directly into the two SIS mixers, resembling a typical 2SB configuration.

The configuration presented is designed to achieve sideband separation. However, implementing this setup necessitates modifications not only to the IF circuit board but also to its module container, the cryostat, and the waveguides.

4.7 Results Closeout

In this section, the entire modification to the IF circuit board is shown. In order to obtain an improved bandwidth, passive components were added to the circuit, the coupled lines filter was eliminated, as well as the radial stubs. This results in a new IF circuit that possesses a 9.3 GHz bandwidth, wider than the previous 4 GHz bandwidth of the CSO receiver.

The calculations made in the mathematical analysis demonstrate that it is not possible to achieve sideband separation with the current design of the circuit, which includes the RF and the LO signals entering the mixers in the same input. This causes the phase of both signals to remain the same regardless of the components added at the IF output. Therefore, a new design for the LO input to the mixer is suggested.

The outcomes obtained in this section are verified in the discussion section, where additional experiments and comparisons are made.

Chapter 5

Conclusions and Future Work

The Leighton Chajnantor Telescope is set to undergo a comprehensive refurbishment in preparation for commencing operations at its new site, situated at an altitude of 5,000 meters on the Llano de Chajnantor. This transition is scheduled to take place within the next few months. Among the planned endeavors is a significant upgrade to the receiver system. Currently, the receiver functions within a 4 GHz bandwidth, a limitation imposed by the design of the IF circuit and the operational range of the low-noise amplifiers. To address this limitation, a modification of this IF circuit has been proposed. This new design aims to enable an expanded bandwidth of 9 GHz, enhancing the telescope's capabilities.

In the present work, we have redesigned the IF circuit board of the Leighton Chajnantor Telescope receiver using High-Frequency Simulation Software (HFSS). It began with the construction of a Technology Demonstration Receiver as an HFSS model, where a comparison with the original circuit was conducted to confirm the model's viability. Some limitations had to be taken into account for the modifications: the board's dimensions needed to remain the same as the original, and minimal changes to the transmission line were necessary to avoid affecting the SIS mixer's performance.

Once these conditions were considered, the modifications began with the addition of passive components and wire bonds to the circuit model. The first step was to eliminate the coupled lines filter and transform it into a transmission line by installing wire bonds. Afterward, a 68 pF capacitor and a 330 Ohm resistor were added to the circuit model in the form of S parameters obtained from the

manufacturer's website and then uploaded to HFSS.

Then, simulations were conducted with the aforementioned modifications in the circuit model, taking approximately 10 minutes to complete. The results of these simulations demonstrated an expanded receiver bandwidth, ranging from 0.06 to 9.3 GHz, which is wider than the previous 4 - 8 GHz bandwidth. This outcome represents a significant advancement towards achieving the overall objective of the LCT, which involves upgrading the receiver's performance.

On the other hand, it was mathematically demonstrated that the implementation of a 2SB configuration in the circuit is not feasible due to the design of the RF and LO signal inputs to the circuit module. Instead, a change in the implementation of the LO signal input in the cryostat and the module was suggested. This alteration would allow the separation of the upper sideband and the lower sideband by integrating a digital 90° hybrid at the IF signal output.

Future work includes the fabrication of the new circuit design proposed in this thesis and conducting measurements with the SIS mixers to ultimately validate the novel design. Finally, this circuit will be integrated into the first light receiver of the Leighton Chajnantor Telescope.

Bibliography

ALMA, O. (2021). Alma capabilities. http://www.almaobservatory.org/. Last accessed 08-10-2022.

ANSYS (2023). Hfss. https://www.ansys.com/. Last accessed 11-08-2023.

Bogatin, E. (2020). *Bogatin's Practical Guide to Transmission Line Design and Characterization for Signal Integrity Applications*. Artech House, Norwood, MA 02062.

Cadence Design Systems, I. (2023). Awr. https://www.cadence.com//. Last accessed 08-08-2023.

Ellingson, S. W. (2018). *Electromagnetics, Vol. 1*. VT Publishing, Blacksburg, VA.

Finger, R., Mena, F., Reyes, N., Rodríguez, R., and Bronfman, L. (2013). A calibrated digital sideband separating spectrometer for radio astronomy applications. *Publications of the Astronomical Society of the Pacific*, 125:263–269.

Friis, H. T. (1944). Noise figures of radio receivers. *Proceedings of the IRE*, 32:419–422.

Golwala, S. (2023). Caltech submillimeter observatory. http://cso.caltech.edu/. Last accessed 08-16-2023.

Iguchi, S. (2005). Radio interferometer sensitivities for three types of receiving systems: Dsb, ssb, and 2sb systems. *Publications of the Astronomical Society of Japan*, 57:643–677.

IPC (2003). *Generic Standard on Printed Board Design IPC-2221A*. Institute for Printed Circuits, Northbrook, Illinois.

Khudchenko, A., Hesper, R., Baryshev, A., Gerlofma, G., Barkhof, J., Adema, J., Mena, F., Klapwijk, T., and Spaans, M. (2012). Sideband separating mixer for 600-720 ghz for alma band 9 upgrade. *Proc SPIE*, 8452:14–.

Kooi, J. (2008). *Advance Receivers for Submillimeter and Far Infrared Astronomy*. PhD thesis, Rijksuniversiteit Groningen.

Kooi, J. W. (June 20, 2005). Balanced and single if measurements cso mixers (3-9 ghz). Technical report, California Institute of Technology.

Kooi, J. W., Chamberlin, R. A., Monje, R. R., Kovács, A., Rice, F., Yoshida, H., Force, B., Cooper, K., Miller, D., Gould, M., et al. (2014). Performance of the caltech submillimeter observatory dual-color 180–720 ghz balanced sis receivers. *IEEE Transactions on Terahertz Science and Technology*, 4(2):149–164.

Kraus, J. D., Tiuri, M., Räisänen, A. V., and Carr, T. D. (1986). *Radio Astronomy*. Cygnus-Quasar Books, 2nd edition.

Lamb, J. W. (2014). Evaluation of biasing and protection circuitry components for cryogenic MMIC low-noise amplifiers. *Cryogenics*, 61:43–54.

Meyers, R. (2002). *Encyclopedia of Physical Science and Technology*. Number v. 12 in Encyclopedia of Physical Science and Technology. Academic Press.

Mini-Circuits (2020). Filters. https://blog.minicircuits.com/. Last accessed 05-15-2023.

Mouser Electronics, I. (2023). Silicon rf capacitors / thin film. http://www.mouser.com/. Last accessed 03-02-2023.

Pozar, D. (2011). *Microwave Engineering*. John Wiley & Sons, 4th edition.

Rodriguez, R. (2015). *Design, construction and testing of a 2SB receiver for the southern millimeter-wave telescope*. PhD thesis, Universidad de Chile.

Skyworks Solutions, I. (2023). Rf passive components. https://www.skyworksinc.com/. Last accessed 02-20-2023.

Wengler, M. (1992). Submillimeter-wave detection with superconducting tunnel diodes. *Proceedings of the IEEE*, 80(11):1810–1826.

Wilson, T., Rohlfs, K., and Huettemeister, S. (2008). *Tools of Radio Astronomy*. Astronomy and Astrophysics Library. Springer Berlin Heidelberg, 5th edition.